Canadian Journal of Earth Sciences
Revue canadienne des sciences de la Terre

Geochemistry, geochronology, and fluid inclusion study of the Late Cretaceous Newton epithermal gold deposit, British Columbia

Journal:	*Canadian Journal of Earth Sciences*
Manuscript ID	cjes-2015-0068.R1
Manuscript Type:	Article
Date Submitted by the Author:	05-Oct-2015
Complete List of Authors:	Liu, Lijuan; University of Alberta, Earth & Atmospheric Sciences Richards, Jeremy P.; Dept of Earth and Atmospheric Sciences DuFrane, S. Andrew; University of Alberta, Earth & Atmospheric Sciences Rebagliati, Mark; Hunter Dickinson Inc.,
Keyword:	Newton, Intermediate sulfidation, Epithermal gold deposit, British Columbia

Geochemistry, geochronology, and fluid inclusion study of the Late Cretaceous Newton epithermal gold deposit, British Columbia

Lijuan Liu, Jeremy P. Richards, S. Andrew DuFrane, Mark Rebagliati

Lijuan Liu (e-mail: lijuan1@ualberta.ca), Jeremy P. Richards* (e-mail: Jeremy.Richards@ualberta.ca), and S. Andrew DuFrane (e-mail: dufrane@ualberta.ca)
Department of Earth & Atmospheric Sciences, University of Alberta, Edmonton, AB, T6G 2E3, Canada
Mark Rebagliati (MarkRebagliati@hdimining.com)
Hunter Dickinson Inc., Vancouver, BC, V6E 4H1, Canada

* Corresponding author: Jeremy P. Richards, Dept. Earth and Atmospheric Sciences
Earth Sciences Building, Rm. 3-02, University of Alberta, Edmonton, Alberta,
Canada, T6G 2E3
Tel: 780-492-3430
Fax: 780-492-2030
E-mail: Jeremy.Richards@ualberta.ca

Abstract

Newton is an intermediate-sulfidation epithermal gold deposit related to Late Cretaceous continental arc magmatism in south-central British Columbia. Disseminated gold mineralization occurs in quartz-sericite-altered Late Cretaceous felsic volcanic rocks, and feldspar-quartz-hornblende porphyry and quartz-feldspar porphyry intrusions. The mineralization can be divided into 3 stages: (1) disseminated pyrite with microscopic gold inclusions, and sparse quartz-pyrite ± molybdenite veins; (2) disseminated marcasite with microscopic gold inclusions and minor base metal-sulfides; and (3) polymetallic veins of pyrite-chalcopyrite-sphalerite-arsenopyrite.

Re-Os dating of molybdenite from a stage 1 vein yielded an age of 72.1 ± 0.3 Ma (McClenaghan 2013). The age of the host rocks has been constrained by U-Pb dating of zircon: Late Cretaceous felsic volcanic rocks: 72.1 ± 0.6 Ma (Amarc Resources Ltd., unpublished data, reported in McClenaghan 2013); feldspar-quartz-hornblende porphyry: 72.1 ± 0.5 Ma; quartz-feldspar porphyry: 70.9 ± 0.5 Ma (Amarc Resources Ltd., unpublished data, reported in McClenaghan 2013). The mineralized rocks are intruded by a barren diorite, with an age of 69.3 ± 0.4 Ma.

Fluid inclusions in quartz–pyrite ± molybdenite ± gold veins yielded an average homogenization temperature of 313° ± 51°C (n = 82) and salinity of 4.8 ± 0.9 wt.% NaCl equiv. (n = 46), suggesting that a relatively hot and saline fluid likely of magmatic origin was responsible for the first stage of mineralization. Some evidence for boiling was also observed in the veins. However, the bulk of the gold mineralization occurs as disseminations in the wallrocks, suggesting that wallrock reactions were the main control on ore deposition.

Keywords: Newton, Intermediate-sulfidation, Epithermal, Gold, British Columbia

Introduction

The Newton gold deposit is a significant new discovery in southern British Columbia. It is located roughly 110 km southwest of Williams Lake at 51°47'N and 123°36' W (Fig. 1). The disseminated Au mineralization in the Newton area is genetically and spatially associated with Late Cretaceous calc-alkaline felsic volcanic rocks and coeval intrusions (Bordet et al. 2011; McClenaghan 2013).

Gold mineralization was first discovered by Mr. Newton in 1916 (Pressacco 2012). The Newton property changed hands several times between 1972–2006, during which time 39 drill holes with a total length of 5762.2 m were completed by Cyprus (10 holes in 1972), Taseko (12 holes in 1982), Rea Gold (5 holes in 1992), and High Ridge (12 holes in 2006) (Pressacco 2012).

The Newton gold deposit was acquired by Amarc Resources Ltd. in 2009, who completed 89 diamond drill holes with a total length of 27 944.5 m between 2009 and 2012. The drilling programs conducted by Amarc successfully intersected Au mineralization, and delineated a new epithermal Au system (McClenaghan 2013). A resource of 111.5 million tonnes with an average grade of 0.44 g/t Au (0.25 g/t Au cut-off) was reported by Pressacco (2012).

The Newton deposit has characteristics of both porphyry and epithermal deposits, and McClenaghan (2013) classified it as an intermediate sulfidation epithermal system. McClenaghan (2013) conducted a petrologic, geochemical, and geochronological study on the deposit, and interpreted the Newton deposit to be an intermediate-sulfidation epithermal deposit based on the classifications of Hedenquist et al. (2000) and Sillitoe and Hedenquist (2003). McClenaghan (2013) noted that Newton matches these descriptions in the following ways: rhyolitic host rocks, quartz-sericite alteration, Au and Ag mineralization, and relatively abundant base-metal sulfides (pyrite, marcasite, sphalerite, and galena). Here we present additional geochemical and geochronological (U-Pb) data, plus fluid inclusion data from the mineralized veins, in order to further characterize the deposit. This work forms as part of a wider study of the geology and geophysical signatures of porphyry-epithermal systems in British Columbia (Hübert et al., in press).

Tectonic History and Regional Geology

Tectonic history of the British Columbian Cordillera

The Cordillera of British Columbia is a complex amalgamation of the ancient North American passive continental margin, several island arcs, and an accretionary wedge, which is overlain by later continental arc volcanosedimentary sequences and glacial tills (Nokleberg et al. 2000, 2005). The Cordillera can be divided into several terranes, including the Alexander, Wrangellia, Stikinia, Cache Creek, Quesnel, and Slide Mountain terranes, which abut the North American craton margin, from west to east (Wheeler et al. 1991; Colpron et al. 2006; Nelson and Colpron 2007; Fig. 1). The Phanerozoic tectonic history of British Columbia can be divided into four stages: (1) A passive continental margin developed on the western edge of Laurentia during the Late Cambrian to the Middle Devonian. (2) The passive margin changed to an active margin when the Panthalassa oceanic plate began to subduct beneath Laurentia in the Middle Devonian; back-arc rifting formed island arcs offshore of the continental margin from the Middle Devonian to Early Jurassic. (3) Several island arcs were accreted to the margin during the Middle Jurassic to Middle Cretaceous. (4) Continental arc magmatism was widespread during the Late Cretaceous to Eocene; the Newton deposit is genetically associated with this Late Cretaceous magmatism in the Stikinia terrane.

During this fourth tectonic phase, oblique convergence between the Kula oceanic plate and North American plate led to compressional and transpressional stress in British Columbia (Engebretson et al. 1985), which resulted in regional deformation, crustal thickening, and uplift (e.g., the Sevier and Laramide orogenies; Gillespie and Heller 1995; English and Johnston 2004). Major displacements occurred along several extensive strike-slip faults during this period, including the dextral Eocene Tintina, Fraser, and Yalakom faults (Gabrielse et al. 2006). Compression and transpression changed to extension and transtension in southern British Columbia in the Eocene (Parrish et al. 1988), probably in response to a change in obliquity of convergence of the Kula oceanic plate (Nokleberg et al. 2000). Continental arc magmatism continued throughout the Late Cretaceous–Eocene, and is related to porphyry and epithermal deposit formation within the accreted terranes, such as the Bulkley intrusive suite (84–64 Ma) and associated porphyry deposits (e.g., Huckleberry, Whiting Creek, and Emerald Glacier; MacIntyre et al. 1994; McMillan et al. 1995; Lepitre et al. 1998; Riddell 2011). Epithermal deposits include Newton, Blackwater, Capoose, Black Dome, Wolf, and Clisbako (Fig. 2; Nelson and Colpron 2007; Mihalasky et al. 2011; Pressacco 2012; McClenaghan 2013). The Newton property is situated between two regional dextral strike-slip faults, the Yalakom fault to the west and the Fraser fault to the east, which were formed by Eocene crustal-scale transtension (Nelson and Colpron 2007; Figs. 1, 2).

Regional geologic setting of the Newton deposit

The Stikinia terrane sequence in the vicinity of the Newton Au deposit is mainly composed of four rock units: volcanic and sedimentary rocks of the Early Cretaceous Spences Bridge and Gambier Groups; the Paleogene Endako and Ootsa Lake Groups;

the Mio-Pliocene Chilcotin Group; and Jurassic to early Tertiary intrusive rocks (Fig. 3; Massey et al. 2005). The Early Cretaceous Spences Bridge Group consists of andesite and dacite lava flows and breccias, minor basalt and rhyolite, pyroclastic deposits, sandstone, siltstone, and mudstone (Massey et al. 2005). This unit is conformably overlain by the Early Cretaceous Gambier Group, which is mainly composed of mafic–intermediate–felsic volcanic, pyroclastic, and sedimentary rocks (Massey et al. 2005). Rhyolite from the Gambier Group yielded a U-Pb age of 112.0 ± 0.3 Ma (Lynch 1995). The Paleogene Endako and Ootsa Lake Groups unconformably overlie the Gambier Group, and consist of mafic to felsic volcanic sequences, and minor sedimentary rocks (Massey et al. 2005).

These sequences are intruded by a wide variety of Jurassic to early Cenozoic dikes and stocks in the Newton area, including felsic porphyry dikes, and quartz monzonite, feldspar-quartz-hornblende porphyry, and diorite stocks (McLaren and Rouse 1989). These rocks are unconformably overlain by the Miocene-Pliocene Chilcotin Group, which mainly consists of basaltic lava flows (Bevier 1983a, 1983b).

Newton Deposit Geology

Quaternary glacial till covers most of the Newton property, and outcrop is sparse. Consequently, geological information has primarily been obtained from drill core. Six main lithological units occur on the property. Layered mafic volcanic rocks are overlain by sedimentary rocks and then felsic volcanic rocks. These layered rocks are intruded by quartz-feldspar porphyry, feldspar-quartz-hornblende porphyry, and diorite intrusions (Riddell 2006; Pressacco 2012). The quartz-feldspar porphyry and feldspar-quartz-hornblende porphyry bodies mainly occur in the center of the Newton deposit, whereas diorite occurs as a large unmineralized intrusion in the northwest corner of the property, and as minor dikes intruding the central quartz-feldspar porphyry and feldspar-quartz-hornblende porphyry (Fig. 4).

The mafic volcanic rocks and sedimentary rocks at Newton have not been dated, but based on regional geological maps (Fig. 3), these rocks are thought to be part of the Lower Cretaceous Gambier Group, which includes similar lithologies. The felsic volcanic rocks and quartz-feldspar porphyry have been dated by zircon U-Pb analysis, and yielded ages of 72.1 ± 0.6 Ma and 70.9 ± 0.5 Ma, respectively (unpublished data, Amarc Resources Ltd., reported in McClenaghan 2013). Gold mineralization at Newton is hosted by these Late Cretaceous felsic volcanic rocks and the quartz-feldspar porphyry and feldspar-quartz-hornblende porphyry intrusions (see below). McClenaghan (2013) reported a Re-Os molybdenite age of 72.1 ± 0.3 Ma for a porphyry-hosted quartz-calcite-pyrite-molybdenite vein, indicating a close temporal relationship between the mineralization and its host rocks.

Mafic volcanic rocks

Mafic volcanic rocks mainly occur in the central part of the Newton deposit. The age of these rocks is not known, but regionally mafic volcanic rocks only occur in the Lower Cretaceous Gambier Group, to which we therefore assign this sequence. This unit is basaltic to andesitic in composition, dark green to dark brown in color, massive in texture, and over 300 m thick on the property (Pressacco 2012). The rocks are mainly composed of volcaniclastic units, lava flows, and volcanic tuff (Fig. 5C), which are epidote-chlorite-altered to varying degrees.

Sedimentary rocks

Cretaceous sedimentary rocks are primarily located in the eastern part of the Newton property (Fig. 4). The unit mainly consists of conglomerates, mudstones, and sandstones (Fig. 5H). Contacts between these sedimentary rocks and the mafic volcanic rocks are mostly faulted such that their stratigraphic relationships are not clear. However, the presence of some mafic volcanic clasts in the conglomerates suggests that these sediments overlie the mafic volcanic sequences (McClenaghan 2013).

Felsic volcanic rocks

Felsic volcanic rocks are mainly located in the central and eastern part of the Newton property, and consist dominantly of felsic tuff (Fig. 5D) with minor coarse-grained felsic volcaniclastic rocks. The felsic volcanic rocks overlie the sedimentary rocks, and unconformable contacts are observed in drill cores (McClenaghan 2013). The felsic volcanic rocks are rhyolitic in composition with calc-alkaline affinity, are white to grey in color, and banded to massive in texture. Most felsic volcanic rocks have undergone strong quartz-sericite alteration, and are the primary host rocks for Au mineralization at Newton.

Intrusive rocks

Quartz-feldspar porphyry: The quartz-feldspar porphyry intrudes the sedimentary and felsic volcanic rocks. It is granitic in composition, and consists of 10–15 vol.% quartz phenocrysts (1–5 mm) and 5–15 vol.% plagioclase phenocrysts (2–5 mm) within a matrix of fine-grained sericite and quartz (<0.05 mm) (Fig. 5E). The porphyry has undergone strong quartz-sericite alteration associated with Au mineralization, and most plagioclase phenocrysts have been replaced by sericite.

Feldspar-quartz-hornblende porphyry: The feldspar-quartz-hornblende porphyry intrudes the sedimentary and felsic volcanic rocks, but no cross-cutting relationships were seen with the quartz-feldspar porphyry. However, cross sections drawn by McClenaghan (2013) show the feldspar-quartz-hornblende porphyry cross-cutting all the sedimentary and volcanic sequences, as well as the quartz-feldspar porphyry. The feldspar-quartz-hornblende porphyry is composed of 20–30 vol.% plagioclase phenocrysts (1–3 mm), 10 vol.% quartz phenocrysts (0.5–2 mm), and 5 vol.% hornblende phenocrysts (1–3 mm) set in a fine-grained quartz-feldspar matrix. Like the quartz-feldspar porphyry, the feldspar-quartz-hornblende porphyry has undergone strong sericitic alteration associated with gold mineralization, and sericite has replaced most of the plagioclase phenocrysts (Fig. 5F).

Diorite: Diorite occurs as a large (>1 km diameter) intrusion to the northwest of the main mineralized zone, and as dikes that cut through the mineralized quartz-feldspar porphyry and feldspar-quartz-hornblende porphyry in the center of the deposit, indicating that it post-dates the main mineralization event. The diorite has undergone propylitic, potassic, and sericitic alteration to varying degrees, but is unmineralized. Relatively fresh diorite (Fig. 5A, B) consists of 30–40 vol.% plagioclase phenocrysts (3–5 mm), 15–20 vol.% hornblende phenocrysts (1–5 mm), and 5 vol.% biotite phenocrysts (1–3 mm) in a fine-grained quartz-plagioclase-hornblende matrix. This unit is weakly to strongly magnetic.

Intrusive breccias: Intrusive breccias locally cut the felsic tuff and porphyry intrusions. They consist of subangular to subrounded fragments of felsic tuff, quartz-feldspar porphyry, and feldspar-quartz-hornblende porphyry in a rhyolitic matrix (McClenaghan 2013). Pressacco (2012) noted that gold mineralization is locally present in the quartz-sericite-altered breccias. The average grade of Au in breccias is 0.2 g/t based on the assay data provide by Amarc Resources Ltd.

Structural setting

Several faults have been identified or inferred on the Newton property, most of which cut the mineralized rocks and therefore post-date mineralization. The Newton Hill Fault is the most significant, and cuts through the main mineralized zone in the eastern part of the property (Fig. 4). This fault strikes approximately 027° and dips at ~30° to the northwest, and displays 300–350 m of dip-slip displacement (Pressacco 2012). Mineralized felsic volcanic rocks, quartz-feldspar porphyry, and feldspar-quartz-hornblende porphyry occur in both the hanging wall and footwall of the fault.

Alteration and Mineralization

Quartz-sericite, argillic, propylitic, and potassic alteration occur at Newton. Quartz-sericite alteration is widespread in the centre of the property, and is closely associated with gold and base metal mineralization.

Quartz-sericite alteration

Quartz-sericite alteration occurs in the felsic volcanic rocks, quartz-feldspar porphyry, and feldspar-quartz-hornblende porphyry (Fig. 6). It is characterized by secondary quartz and sericite, which replace volcanic glass shards, volcanic fragments, and plagioclase, and infill small fractures. The quartz-sericite alteration is most strongly developed in the felsic volcanic rocks, whereas it is relatively weak in the quartz-feldspar porphyry and feldspar-quartz-hornblende porphyry (McClenaghan 2013). This may reflect the higher permeability and reactivity (fine-grained, possibly originally glassy groundmass) of the felsic volcanic rocks compared with the quartz-feldspar porphyry and feldspar-quartz-hornblende porphyry (McClenaghan 2013). This alteration style is only locally present in the diorite (Fig. 7A, B).

The quartz-sericite alteration can be divided into two stages:

1. The first stage predominantly consists of quartz, sericite, and pyrite (Fig. 5D, E), and is associated with gold mineralization (mostly as microscopic inclusions of electrum in disseminated pyrite).
2. The second stage is similar but contains more marcasite than pyrite (Fig. 5F), accompanied by base metal sulfides (sphalerite and chalcopyrite; Fig. 5F).This stage is also associated with gold mineralization (microscopic inclusions in disseminated marcasite and pyrite) but with lower grades than stage 1.

Argillic alteration

Argillic alteration is not extensively developed at Newton, and was only observed locally in the quartz-feldspar porphyry and feldspar-quartz-hornblende porphyry where it overprints the quartz-sericite alteration (Fig. 5G). It is characterized by kaolinite, sericite (relict from the earlier alteration), and carbonates (McClenaghan 2013), which partially or completely replace plagioclase phenocrysts. Minor amounts of gold are locally reported in assay from argillic-altered rocks (McClenaghan 2013), but it is not clear whether the Au was introduced during the argillic alteration, or is residual from the earlier quartz-sericite alteration.

Propylitic alteration

Propylitic alteration is characterized by secondary epidote, chlorite, and carbonate (Fig. 5A, C). Epidote and chlorite are dominant and pervasive, whereas calcite typically occurs in veinlets. This alteration is widespread but variably developed in the mafic volcanic rocks, and is locally present in the diorite (Fig. 7C). Gold and base metal mineralization do not occur in propylitic-altered rocks.

Potassic alteration

The least common alteration type observed at Newton is potassic alteration, which is characterized by the local development of fine-grained secondary biotite and minor pyrite in diorite at its contacts with mafic volcanic rocks (Fig. 7D; Pressacco 2012). Locally, the potassic alteration is overprinted by sericite, and propylitic alteration commonly overprints both potassic and sericitic alteration within the diorite (Fig. 5). Potassic-altered rocks are not associated with economic mineralization at the levels explored to date by drilling.

Mineralization

Metallic minerals at Newton consist of pyrite, marcasite, chalcopyrite, sphalerite, pyrrhotite, molybdenite, arsenopyrite, electrum, and Ag-Au and Au-Bi tellurides (in approximate order of abundance; McClenaghan 2013). The gold-bearing minerals mainly occur as inclusions in sulfides, especially pyrite and marcasite (Pressacco 2012). Disseminated mineralization is the predominant style; veinlet mineralization is also present, but it accounts for less than 1 vol.% of the mineralized rocks (Pressacco 2012).

Three stages of mineralization have been recognized based on observations of hand samples and polished thin sections (Fig. 8).

1. The earliest stage of Au mineralization is associated with quartz-sericite-pyrite wallrock alteration. The dominant sulfide is disseminated pyrite, which is

accompanied by minor chalcopyrite, pyrrhotite, and sphalerite, commonly as small inclusion in pyrite (Fig. 9A). Gold mainly occurs as inclusions of electrum, silver-gold telluride, and gold-bismuth telluride in the pyrite (Fig. 9B; Pressacco 2012). Veins are not common, but where present consist of pyrite (Fig. 5D), quartz-pyrite (Fig. 5E), and quartz-molybdenite-pyrite (Fig. 9C), which are relatively straight and 1–3 mm in width.

2. Stage 2 mineralization is associated with the later quartz-sericite-marcasite alteration. Disseminated marcasite, minor pyrite, chalcopyrite, and sphalerite occur in the felsic volcanic and intrusive rocks (Fig. 9D, E; McClenaghan 2013). Base metal-sulfides are more abundant than in stage 1 (McClenaghan 2013). Although disseminated mineralization is dominant, minor marcasite veinlets also occur in quartz-sericite-marcasite-altered rocks (Fig. 5F). These veinlets are relatively straight, and usually 1–2 mm in width. Pressacco (2012) noted that Au occurs as electrum inclusions in marcasite, but this was not observed in this study.
3. Polymetallic veins occur locally in the sedimentary and felsic volcanic rocks, but are not common. They represent the last stage of mineralization, and cross-cut the disseminated quartz-sericite-pyrite/marcasite mineralization (Fig. 5H). Pyrite, chalcopyrite, sphalerite, and arsenopyrite are primary constituents of these veins, commonly with calcite (Figs. 9F, 5H). These veins are 1–10 mm in width, and are commonly straight but with various orientations; they lack alteration selvages. No gold has been reported in these veins.

Previous metallogenic studies

Molybdenite from a stage 1 quartz-molybdenite-pyrite vein in the feldspar-quartz-hornblende porphyry has been dated at 72.1 ± 0.3 Ma (McClenaghan 2013), indicating that the mineralization occurred broadly at the same time as magmatism.

McClenaghan (2013) also reported oxygen isotopic compositions ($\delta^{18}O$) of 8.4 to 9.5‰ and hydrogen isotopic compositions (δD) of -83.0 to -66.5‰ for sericite associated with auriferous pyrite and marcasite, and calculated $\delta^{18}O_{fluid}$ and δD_{fluid} compositions of 2.5‰ to 6.8‰, and -63 to -46.5‰, respectively, suggesting a predominantly magmatic origin for the fluid. Similarly, sulfur isotopic compositions of disseminated pyrite, marcasite, and chalcopyrite range from $\delta^{34}S$ = -1.1 to 3.2‰, consistent with a magmatic source for sulfur (McClenaghan 2013).

McClenaghan (2013) interpreted the Newton deposit to be an intermediate-sulfidation epithermal deposit based on the classifications of Hedenquist et al. (2000) and Sillitoe and Hedenquist (2003). McClenaghan (2013) noted that Newton matches these descriptions in the following ways: rhyolitic host rocks, primary quartz-sericite alteration, Au and Ag mineralization, and relatively abundant base-metal sulfides (pyrite, marcasite, sphalerite, and galena).

Analytical methods

Sample selection

Twenty-eight drill core samples were collected for this study, which are representative of the country rocks, intrusions, alteration facies, and mineralization styles at Newton. Detailed information on these samples is listed in Table A1, and sampled drill holes are marked on the geological map in Figure 4. All the drill holes sampled were vertical. Fifteen polished thin sections were made for petrographic study, and 5 fluid inclusion sections were made from quartz-sulfide and carbonate-sphalerite veins for fluid inclusion study.

Lithogeochemical analysis

Five feldspar-quartz-hornblende porphyry and five diorite samples were collected for whole-rock geochemical analysis. Lithogeochemical analyses were conducted at Activation Laboratories Ltd. (Ancaster, Ontario, Canada) using a combination of methods including instrumental neutron activation analysis and lithium metaborate/tetraborate fusion inductively coupled plasma mass spectrometry (Actlabs code 4E Research + ICP/MS). Based on reproducibility of standards and duplicates, accuracy is typically within 5 relative percent for major elements, and 10 relative percent for minor and trace elements.

Zircon U-Pb dating

Zircon crystals were separated from two samples of drill core with lengths of 1–2 m by crushing, Wilfley table heavy mineral separation, magnetic separation, heavy-liquid separation, and handpicking. Selected crystals were mounted in epoxy, and polished to expose their cores. They were then analyzed using a Nu-Plasma multi-collector inductively coupled plasma-mass spectrometer (MC-ICP-MS; Nu Instruments, UK) coupled to a frequency quintupled ($\lambda = 213$ nm) Nd:YAG laser ablation system (New Wave Research, USA) in the Radiogenic Isotope Facility at the University of Alberta. Details of the analytical setup and protocols employed are described in Simonetti et al. (2005). Laser pit dimensions were 30 μm diameter and approximately 20–30 μm deep. A 30 s blank analysis prior to ablation was made for determination of ^{204}Hg contributions, and was followed by 30 s ablations on samples.

Zircon reference materials GJ1-32 and LH94-15 were used to correct instrumental bias, drift, and laser induced U-Pb fractionation. Standards were analyzed after every ten unknowns, and the 2σ reproducibility of the standards was ~3% for U/Pb and 1% for $^{207}Pb/^{206}Pb$. Reported errors are a quadratic combination of the within-run precision and the external reproducibility of the standards. All U-Pb plots were generated using the Isoplot software (Ludwig 2003), and concordia intercept ages were derived by anchoring to a common Pb value of 0.83 ± 0.06 (Stacey and Kramers 1975).

Fluid inclusion measurements

Fluid inclusion measurements were conducted using a Linkham THMSG600 microthermometric stage mounted on an Olympus BX50 microscope. Fluid inclusions were cooled to -100°C, and then final ice melting temperatures, clathrate melting temperatures, and total homogenization temperatures were recorded during reheating. The salinities of aqueous, CO_2 clathrate-bearing, and halite-bearing inclusions were calculated using final ice melting, final CO_2 clathrate melting, and halite dissolution temperatures, based on the equations of Bodnar (1993), Bozzo et al. (1975), and Sterner et al. (1988), respectively. Bozzo et al. (1975) noted that their equation strictly applied only to fluid inclusions that contained liquid CO_2 at the point of clathrate melting, but Diamond (1992) noted that the presence or absence of a CO_2 liquid phase actually had little effect on salinity calculations. Liquid CO_2 was not observed in our fluid inclusions, but on the basis of Diamond's (1992) findings, we have used Bozzo et al.'s (1975) equation for salinity estimation in clathrate-bearing inclusions. Synthetic fluid inclusion standards from Syn Flinc were used for calibration: reported measurements are accurate to ±0.2°C below 10°C, and ±2°C above 10°C.

Fluid inclusions were classified as primary, pseudosecondary, and secondary based on the criteria of Roedder (1984) and Goldstein (2003), and were grouped in fluid inclusion assemblages (Goldstein and Reynolds 1994; Goldstein 2003).

Geochemical Compositions of Igneous Rocks

Ten new whole-rock geochemical analyses of feldspar-quartz-hornblende porphyry and diorite are listed in Table 1. These analyses are combined with 21 analyses of felsic volcanic rocks and quartz-feldspar porphyry reported by McClenaghan (2013) to assess the compositional range and geochemical affinity of the Newton igneous suite. All of the samples show some degree of alteration, but selected samples showed the least alteration of available material.

Major element compositions and lithological classification

Major element data for igneous rock samples from the Newton deposit were recalculated on a volatile-free basis, and plotted on a total alkali–silica classification diagram (Fig. 10). Diorite samples plot in the diorite to granodiorite fields, feldspar-quartz-hornblende porphyry samples plot in the granodiorite and granite fields, and quartz-feldspar porphyry samples plot in the granite field. The felsic volcanic rocks plot almost exclusively in the granite (rhyolite) field. McClenaghan (2013) identified two samples of felsic volcanic rock and quartz-feldspar porphyry as “least altered” (based on geochemical and petrographic criteria, such as containing largely unaltered plagioclase phenocrysts), but all other samples show moderate to strong degrees of alteration (mostly sericitic). Because all of the samples plotted here are altered to varying degrees, caution must be exercised when using the total alkali–silica diagram for lithological classification purposes. However, the data plot fairly tightly, and the compositions of the two least-altered volcanic and quartz-feldspar porphyry samples are similar to more altered equivalents. We therefore consider that alteration has not affected these rocks to a degree that would change their broad lithological classification. On this basis, the data suggest a typical calc-alkaline trend from dioritic to granitic compositions for the intrusive rocks, and predominantly rhyolitic compositions for the volcanic rocks (Peccerillo and Taylor 1976; Fig. 10).

Concentrations of TiO_2, MgO, and P_2O_5 are plotted relative to SiO_2 in Figure 11A–C, and show reasonably well correlated inverse trends, suggesting a cogenetic relationship though fractionation of ferromagnesian silicates, magnetite, and apatite. Potassium shows greater scatter relative to SiO_2, likely due to the effects of hydrothermal alteration, but the data nevertheless group within the calc-alkaline to high-K calc-alkaline fields in Figure 11D, consistent with a volcanic arc origin.

Trace element compositions

Due to varying degrees of hydrothermal alteration at Newton, plots using immobile elements Y, Yb, Ta, Nb, are used for tectonic discrimination (Fig. 12). All samples plot in the field of volcanic arc rocks.

Trace element data for igneous rock samples from the Newton deposit are plotted on primitive mantle-normalized trace element and chondrite-normalized rare earth element (REE) diagrams in Figures 13 and 14. The samples display broadly similar patterns on primitive mantle-normalized trace element diagrams (Fig. 13), with relative enrichments in incompatible large-ion lithophile elements (LILE) and distinctive depletions in Nb, Ta, and Ti, characteristic of arc-related magmas (Gill 1981; Briqueu et al. 1984; Brown et al. 1984). The suite also shows depletions in Sr and P, which, along with Ti, are more pronounced in the felsic volcanic rocks, reflecting fractionation of feldspar, apatite, and magnetite, respectively. The more mafic diorites show positive anomalies for Sr, which may indicate minor plagioclase feldspar accumulation. The diorites also have higher concentrations of compatible elements such as middle and heavy REE (MREE, HREE) compared to the more evolved rocks.

On chondrite-normalized rare earth element diagrams (Fig. 14), the quartz-feldspar porphyry, feldspar-quartz-hornblende porphyry, and felsic volcanic rock samples show listric-shaped REE patterns (steep slopes from light REE (LREE) to MREE, and shallow to flat slopes from MREE to HREE; La/Yb = 11.7 to 36.0), suggesting that amphibole fractionation was important (Sisson 1994). In contrast, the diorite samples show slightly shallower slopes from LREE to MREE, and flat slopes from MREE to HREE, consistent with their less evolved compositions relative to the felsic rocks (La/Yb = 4.6 to 23.6).

The more felsic rocks (quartz-feldspar porphyries and volcanic rocks) display small negative Eu anomalies (Figs. 14 and 15), indicative of feldspar fractionation. The lack of significant negative Eu anomalies in the more mafic lithologies (Figs. 14A and 15) indicates that plagioclase fractionation was not important during early crystallization of the parental magmas, but small positive anomalies for some diorite samples are consistent with some later-stage plagioclase accumulation, as also indicated by elevated Sr concentrations (Fig. 13A).

Zircon U-Pb dating

The felsic volcanic rocks and quartz-feldspar porphyry have been dated by Amarc Resources Ltd. (reported in McClenaghan 2013). The felsic volcanic rock sample yielded a weighted mean $^{206}Pb/^{238}U$ age for two zircon grains of 72.1 ± 0.6 Ma

(2σ error; McClenaghan 2013). The quartz-feldspar porphyry sample yielded a weighted mean $^{206}Pb/^{238}U$ age of 70.9 ± 0.5 Ma (MSWD = 1.8; McClenaghan 2013). In order to better understand the relationships between the felsic volcanic rocks and the three phases of intrusions (diorite, feldspar-quartz-hornblende porphyry, quartz-feldspar porphyry), the feldspar-quartz-hornblende porphyry and diorite were dated in this study. The feldspar-quartz-hornblende porphyry sample was collected from drill hole 10031 (Fig. 4) at a depth of 320 m, and the diorite sample was collected from drill hole 10023 (Fig. 4) at a depth of 146 m.

The analyzed zircons are clear, colorless, euhedral, and prismatic, which are characteristic features of magmatic zircons. Oscillatory zoning is well developed in zircons from the diorite (as seen in backscattered electron SEM images; Fig. 16), whereas zircons from the feldspar-quartz-hornblende porphyry are largely unzoned. Variations in the brightness of the different zones are attributed to different proportions of trace elements such as Hf, Y, and REE (Hoskin 2000).

U-Pb dating results for zircons from the feldspar-quartz-hornblende porphyry (NT129) and diorite (NT090) are listed in Table 2 and plotted on Tera-Wasserburg diagrams in Figure 17 (Tera and Wasserburg 1972). The feldspar-quartz-hornblende porphyry sample contains a relatively homogeneous population of concordant zircons, which yielded a U-Pb concordia intercept age of 72.1 ± 0.5 Ma (n = 25, MSWD = 1.4; Fig. 17A). The diorite sample contains a slightly more complicated population of zircons, which yielded a U-Pb concordia intercept age of 69.3 ± 0.4 Ma (n = 21, MSWD = 1.5; Fig. 17B). A $^{238}U/^{206}Pb$ age histogram for the diorite zircons (Fig. 18) suggests the presence of two populations of zircon in the diorite sample, one with an age close to the bulk sample at ~69 Ma, and a smaller group with slightly older ages ~71 Ma. This older group is similar to the ages of the feldspar-quartz-hornblende porphyry and felsic volcanic rocks, and may represent xenocrystic or antecrystic zircon inherited from slightly earlier intrusions within the same magmatic complex. Alternatively, the younger (~69 Ma) ages may reflect minor Pb-loss, and the true age of the diorite may be essentially coeval with the other igneous rocks at ~71 Ma.

Fluid inclusions

Quartz veins are not common at Newton. Measurable primary and pseudosecondary fluid inclusions were only found in two quartz vein samples, which are both related to stage 1 mineralization. One sample is a quartz-pyrite vein (with electrum inclusions in pyrite) hosted by quartz-feldspar porphyry (sample NT049) from borehole 9004 at a depth of 270 m. The other sample is a quartz-molybdenite-pyrite vein hosted by felsic volcanic rocks (sample NT060) from borehole 12057 at a depth of 200 m. No quartz veins related to stage 2 mineralization were found, and sphalerite from a stage 3 polymetallic sulfide vein mineralization was too opaque to observe fluid inclusions.

Ninety-six quartz-hosted fluid inclusions were analyzed. Only primary and pseudosecondary inclusions were analyzed (Fig. 19; criteria of Roedder 1984, and Goldstein 2003), and necked or leaked inclusions were avoided. Primary inclusions were mostly observed in growth zones, whereas pseudosecondary inclusions occur in micro-fractures developed during crystal growth. Measured inclusions ranged in size between 3–7 μm with a few up to 10 μm. Most fluid inclusions are present in groups as fluid inclusion assemblages, in which the vapor/liquid phase ratios are constant (Fig. 19A; Goldstein and Reynolds 1994; Goldstein 2003). A few fluid inclusions occurred as larger isolated inclusions (10-13 μm), which are interpreted to be primary in origin.

Three distinct fluid inclusion types were recognized. Type 1 inclusions are two-phase liquid-rich inclusions, and occur in both samples. CO_2 was not seen as a separate liquid or vapor phase, and no melting events were observed at -56.6°C during heating that would indicate the presence of CO_2. However, some inclusions displayed melting events at temperatures above 0°C, indicating that small amounts of CO_2 are present as CO_2 clathrate. Therefore the type 1 inclusions can be subgrouped into type 1a inclusions (without CO_2 clathrate) and type 1b inclusions (with CO_2 clathrate).

Type 2 inclusions are two-phase vapor-rich inclusions, and also occur in both samples. It is difficult to observe phase changes in these predominantly dark inclusions, and no microthermometric data could be obtained (cf. Bodnar et al. 1985). Primary type 2 inclusions occur together with liquid-rich type 1 inclusions in one fluid inclusion assemblage from the quartz-pyrite-gold vein (NT049), and this is taken to be evidence that boiling occurred in this vein sample (Fig. 19C). Boiling also likely occurred in the other quartz-molybdenite-pyrite vein, as evidenced by the presence of type 2 vapor-rich fluid inclusions in this sample (NT060). However, they were not observed in the same assemblages as type 1 inclusions, so the identification of boiling is not definitive for this sample.

Type 3 fluid inclusions contain three or four phases, including halite and in some cases opaque daughter minerals, in addition to liquid and vapor phases (Fig. 19B). Halite crystals were recognized by their cubic morphology and relatively slow dissolution during heating. Type 3 inclusions are rare, and only occur locally at the edges of the quartz-molybdenite-pyrite vein (NT060). Type 3 inclusions are therefore thought to represent early stage fluids.

Homogenization temperature and salinity measurements

Microthermometric measurements and salinity estimates for fluid inclusions are presented in Figures 20 and 21, and listed Table A2.

Quartz-pyrite-gold vein sample (NT049): Type 1a fluid inclusions from the quartz-pyrite-gold vein sample homogenized by bubble disappearance at temperatures ranging from 210° to 415°C (average = 327° ± 48°C; n = 47). Fluid salinities for type 1a inclusion (as measured from ice melting temperatures) range from 4.0 to 6.0 wt.% NaCl equiv. (average = 5.2 ± 0.7 wt.% NaCl equiv., n = 24).

Type 1b inclusions from this sample homogenized at similar temperatures to type 1a inclusions (316° to 355°C; average = 343° ± 15°C, n = 6). Salinities calculated from clathrate melting temperature are more scattered because of the lower precision of this method (0.8 to 7.1 wt.% NaCl equiv.; average = 4.0 ± 2.4 wt.% NaCl equiv., n = 6), but overlap the tighter range of type 1a inclusions.

The homogenization temperatures and salinities of type 2 vapor-rich fluid inclusions could not be measured due to the small amount of liquid present, but type 1a inclusions in the same assemblage range from 293°–369°C (average = 329° ± 32°C, n = 7) and 4.3–6.0 wt.% NaCl equiv. (average = 5.3° ± 0.6°C, n = 7).

Quartz-molybdenite-pyrite vein sample (NT060): Type 1a fluid inclusions from the quartz-molybdenite-pyrite vein sample homogenized by bubble disappearance at temperatures ranging from 205° to 388°C (average = 294° ± 49°C; n = 35). Fluid salinities for type 1a inclusion range from 2.9 to 6.4 wt.% NaCl equiv. (average = 4.5 ± 1.0 wt.% NaCl equiv., n = 22).

Type 1b inclusions from this sample homogenized at similar temperatures to type 1a inclusions (241° to 389°C; average = 314° ± 71°C, n = 4). Salinities calculated from clathrate melting temperature also overlap (at the lower end) the range for type 1a inclusions (2.8 to 4.7 wt.% NaCl equiv.; average = 3.8 ± 0.9 wt.% NaCl equiv., n = 4).

Rare type 3 hypersaline fluid inclusions occur in quartz at the vein margin. They homogenized finally by halite daughter crystal dissolution at temperatures ranging from 335° to 355°C (average = 343° ± 9°C; n = 4), indicating salinities of (34.2 to 35.1 wt.% NaCl equiv.; average = 34.8 ± 0.5 wt.% NaCl equiv., n = 4). The vapor bubble disappeared at lower temperatures (244°–260°C; average = 255° ± 8°C; n = 4).

Homogenization temperature-salinity data from a quartz-molybdenite-pyrite vein show a trend from a relatively high temperature and saline composition (370°C; 5.7 wt.% NaCl equiv.) to a lower temperature and less saline fluid (205°C; 3.1 wt.% NaCl equiv.; Fig. 21). This trend is not observed in individual fluid inclusion assemblages, indicating that in situ fluid mixing was not occurring. Instead, the trend can be correlated with vein paragenesis, with high temperature and salinity (including hypersaline) fluid inclusions occurring only near the vein margins, and lower temperature and salinity fluid inclusions occurring toward the vein centers.

Pressure estimates

Because there is evidence of boiling in one vein sample, homogenization temperatures are assumed to be close to the real trapping temperatures for most of the type 1 fluid inclusions, and no pressure corrections have been made to homogenization temperatures (Roedder and Bodnar 1980; Bodnar and Vityk 1994). The average homogenization temperature and fluid salinity of all type 1a inclusions is 313° ± 51°C (n = 82), and 4.8 ± 0.9 wt.% NaCl equiv. (n = 46). Therefore assuming that the hydrothermal fluid is a pure H_2O-NaCl system with a temperature of ~310°C and salinity of ~5 wt.% NaCl equiv., the trapping pressure for fluid inclusions related to stage 1 mineralization can be estimated to be ~95 bars, equivalent to a depth of around 1160 m (assuming hydrostatic pressure conditions) based on the data of Haas (1971). However, the presence of small amounts of CO_2 in some type 1b inclusions may mean that fluid pressures (and therefore depths) were slightly greater.

Trapping pressure of type 3 inclusions were estimated using the program HOKIEFLINCS_H2O-NaCl (Steele-MacInnis et al. 2012), and yielded values of 98 to 125 bar (average = 108 bar, n = 4), consistent with the estimates from boiling assemblages. A trapping depth of ~1 km is therefore considered reasonable based on these data.

Discussion

Timing and petrogenesis

The felsic volcanic rocks, feldspar-quartz-hornblende porphyry, quartz-feldspar porphyry, and post-mineralization diorite stock at Newton yielded U-Pb zircon ages of 72.1 ± 0.6 Ma, 72.1 ± 0.5 Ma, 70.9 ± 0.5 Ma, and 69.3 ± 0.4 Ma respectively (McClenaghan 2013; this study). These ages indicate that the magmatic activity at Newton is broadly coeval, and spanned a time period of ~ 3 m.y. (~72–69 Ma), or possibly only ~1 m.y. if the true age of the diorite is closer to 71 Ma, as suggested by the bimodal population of zircon ages for this samples (the younger ages ~69 Ma reflecting minor Pb-loss). A single Re-Os date on hydrothermal molybdenite (72.1 ± 0.3 Ma) reported by McClenaghan (2013), is consistent with the ages of the felsic volcanic rocks and feldspar-quartz-hornblende porphyry, but is slightly older than the age of the main quartz-feldspar porphyry host rock. This slightly inconsistent result cannot be explained at this time, but may relate to problems comparing data from two different geochronological systems, and also to the difficulty of resolving minor Pb-loss in young samples dated by LA-ICP-MS. Broadly, however, the molybdenite age is consistent with a cogenetic relationship between the magmatic and hydrothermal activity at ~72 Ma.

The felsic volcanic rocks, quartz-feldspar porphyry, feldspar-quartz-hornblende porphyry, and diorite are also broadly cogenetic in terms of their geochemical compositions, and they are assumed to have been derived from the same parent magma. Because the most mafic rock, diorite, is the youngest intrusion, the data cannot be modelled as a simple fractionation trend. However, the diorite is likely reflective of the composition of the more mafic end-member in this suite, and the more evolved lithologies may have evolved from a similar, earlier dioritic magma at depth.

The diorite contains hornblende phenocrysts, which indicate that the magma contained at least 4 wt.% H_2O (Naney 1983). High magmatic water contents can suppress early crystallization of plagioclase, which is evidenced by the absence of europium anomalies in the normalized REE patterns for the diorites (because plagioclase preferentially partitions Eu^{2+} relative to Eu^{3+} and other REE; Hanson 1980). However, the absence of Eu anomalies can also be explained by relatively oxidizing conditions, under which Eu is mainly present as Eu^{3+} (and is therefor not partitioned into plagioclase). Thus, the diorites are interpreted to be either relatively hydrous or oxidized, or both, which are favorable characteristics for the formation of porphyry and related epithermal deposit (Candela 1992; Richards 2003).

Immobile trace element and major element compositions suggest that the Newton igneous suite is of calc-alkaline, continental arc affinity, with compositions ranging from diorite to granite. Listric-shaped REE patterns combined with the lack of europium anomalies in more mafic rocks suggest that the suite was hydrous, and evolved by early fractionation of amphibole (± titanite; Gromet and Silver 1983; Green and Pearson 1985; Rollinson 1993).

Characteristics of ore-forming fluids

Fluid inclusions from two vein samples from stage 1 mineralization record similar temperatures and salinities. Data for type 1a two-phase (liquid + vapor) inclusions from a quartz-sericite-pyrite vein indicate an average homogenization temperature of 327° ± 48°C (n = 47) and salinity of 5.2 ± 0.7 wt.% NaCl equiv. (n = 24). Data from the quartz-molybdenite-pyrite vein overlap this range but show a trend from early inclusions near the vein margin with homogenization temperatures of ~370°C and salinities of ~5.7 wt.% NaCl equiv., and later inclusions near the vein centre with ~205°C and 3.1 wt.% NaCl equiv.; Fig. 21); rare hypersaline fluid inclusions also occur near the vein margin. These data are interpreted to reflect evolution of the fluid in this vein from high temperature and salinity fluids, to cooler, lower salinity compositions.

The presence of vapor-rich fluid inclusions in some assemblages indicates that trapping conditions were at or near the two-phase boundary, and homogenization temperatures of type 1 fluid inclusions have therefore not been corrected for pressure. Pressure estimates from these inclusions, and also from hypersaline inclusions, suggest values ~100 bars, and depths of trapping ~1 km (assuming hydrostatic pressure conditions).

McClenaghan (2013) calculated the isotopic composition of hydrothermal fluids in equilibrium with sericite, and reported $\delta^{18}O_{fluid}$ values ranging from 5.7 to 6.8‰ (average = 6.0 ± 0.4‰, n = 6), and δD_{fluid} from -55.8 to -46.5‰ (average = 51.0‰ ±

3.8, n = 6). Combined with the S isotopic composition of sulfides from stage 1 mineralization ($\delta^{34}S$ = 1.2 to 3.2‰; average = 2.1 ± 0.6‰, n = 10), McClenaghan (2013) concluded that the fluids and sulfur associated with ore formation at Newton were of magmatic origin. Our fluid inclusion data, and especially the observation of hypersaline fluid inclusions, are consistent with this conclusion.

Newton has been classified as an intermediate-sulfidation epithermal gold deposit (McClenaghan 2013), although the quartz-sericite alteration and relatively high fluid temperatures place it in the deeper parts of the spectrum of epithermal deposits, close to the porphyry environment. This interpretation is supported in this study by the observation of porphyry-like halite-bearing fluid inclusions in stage 1 veins, and the presence of potassic alteration in the diorite. Therefore, we propose that the Newton deposit formed near the transition zone between porphyry and epithermal environments. This interpretation implies the potential for porphyry-type mineralization at depth below the currently explored levels, as also suggested by geophysical data (Hübert et al. in press).

Ore depositional processes

Gold is mainly present as inclusions in disseminated pyrite and marcasite in quartz-sericite alteration, and auriferous veins are relatively rare. Consequently, wall rock reactions appear to be the main controls on the precipitation of gold from the magmatic hydrothermal fluids, although minor gold may have been precipitated during boiling in the rare quartz-sulfide veins observed. If it is assumed that gold was dissolved as bisulfide complexes (e.g., $Au(HS)_2^-$; Seward 1989, 1991), then wallrock sulfidation reactions may have been responsible for the coprecipitation of gold with pyrite and marcasite, through reactions such as:

$FeO_{(wallrock)} + 2\ H_2S + ½\ O_2 = FeS_2 + 2\ H_2O$ (eq. 1)

$2\ Au(HS)_2^- + FeO_{(wallrock)} + 2\ H^+ = 2\ Au + FeS_2 + 2\ H_2S + H_2O$ (eq. 2) (Mikucki 1998)

Newton compared with other intermediate-sulfidation epithermal deposits

Epithermal deposits can be classified into high-, intermediate-, and low-sulfidation types in terms of their sulfidation state (Hedenquist et al. 2000; Einaudi et al. 2003; Sillitoe and Hedenquist 2003). The main characteristics of the Newton deposit are compared with Sillitoe and Hedenquist's (2003) description of intermediate-sulfidation (IS) epithermal deposit in Table 3, and key similarities include:

1. The Newton deposit is genetically related to calc-alkaline andesitic-rhyolitic arc magmas.
2. The main wallrock alteration mineral at Newton is sericite.
3. Sulfide abundance in mineralized rocks at Newton is ~2 to 6%.
4. Key sulfide minerals are pyrite, marcasite, sphalerite, galena, and minor chalcopyrite.
5. The main metal enrichments are Ag, Au, Cu, Zn, and Pb, with minor Mo and As.
6. Telluride minerals locally occur as inclusions in pyrite and marcasite.
7. Magmatic fluids were primarily responsible for mineralization at Newton.

Newton differs to some extent from typical IS deposits in being dominated by disseminated mineralization, whereas vein type mineralization is more common in other deposits (Sillitoe and Hedenquist 2003). The disseminated mineralization style at Newton might be related to the transpressional tectonic setting thought to have prevailed at the time of its formation (Nelson and Colpron 2007), leading to more dispersed mineralization styles. Similar disseminated IS-type mineralization is found in the San Cristobal deposit in the Altiplano of Bolivia, which is interpreted to have formed in a compressional tectonic setting (Lamb et al. 1997; Buchanan 2000; Sillitoe and Hedenquist 2003). In contrast, IS deposits formed in extensional tectonic environments tend to be vein or breccia-hosted, such as the Arcata deposit in Peru, and the Fresnillo deposit in Mexico (Noble et al. 1990; Albinson et al. 2001; Sillitoe and Hedenquist 2003).

Two other IS Au-Ag deposits of similar age and disseminated mineralization style occur in the southern Stikinia terrane of central British Columbia: the Blackwater and Capoose deposits (Fig. 2; Bordet et al. 2013; McClenaghan 2013). The timing of magmatism and mineralization at these three deposits is similar (72 to 67 Ma), suggesting a pulse of transpression-related magmatism and mineralization in this region in the Late Cretaceous (Andrew 1988; Lane and Schroeter 1997; Friedman et al. 2001; Christie et al. 2014).

The Newton deposit appears to be transitional to underlying porphyry type alteration (and potentially mineralization), as indicated by the presence of rare hypersaline fluid inclusions in early vein stages, the local presence of potassic alteration, and geophysical data (Hübert et al. in press). This is consistent with the commonly observed spatial and genetic relationship between shallow IS and deeper porphyry systems, such as the coupled Acupan and Antamok IS and the Ampucao porphyry deposits in the Baguio district, and the Victoria IS and Far Southeast porphyry deposits in the Mankayan district of the Philippines (Cooke et al. 1996, 2011; Chang et al. 2011).

Conclusions

The Newton epithermal deposit is hosted by a Late Cretaceous volcanoplutonic complex with continental arc affinity, and consists of felsic volcanic rocks (72.1 ± 0.6 Ma; Amarc Resources Ltd., unpublished data, reported in McClenaghan 2013) intruded by coeval quartz-feldspar porphyry (70.9 ± 0.5 Ma; Amarc Resources Ltd., unpublished data, reported in McClenaghan 2013) and feldspar-quartz-hornblende porphyry (72.1 ± 0.5 Ma; this work) stocks and dikes, and a late diorite body (69.3 ± 0.4 Ma; this work). The timing of gold mineralization was constrained by Re-Os dating of molybdenite in a quartz-pyrite-molybdenite vein at 72.1 ± 0.3 Ma (McClenaghan 2013). Gold is mainly present as electrum and gold-silver tellurides in disseminated pyrite and minor marcasite associated with quartz-sericite alteration in the felsic volcanic rocks and porphyries. Three stages of mineralization are recognized: stage 1 disseminate pyrite with gold and minor quartz-pyrite ± molybdenite veins; stage 2 disseminated marcasite with gold; and stage 3 polymetallic-sulfide-carbonate veins (pyrite-chalcopyrite-sphalerite-arsenopyrite-calcite). Stages 1 and 2 are related to quartz-sericite alteration, whereas the stage 3 veins cut across quartz-sericite altered rocks, and lack noticeable alteration selvedges. New fluid inclusion data combined with stable isotope data from McClenaghan (2013) indicate that a relatively hot and saline fluid (~313°C, ~4.8 wt.% NaCl equiv.) of probable magmatic origin was likely responsible for the first stage of mineralization. The coprecipitation of gold with pyrite/marcasite in the sericitized wallrocks likely reflects wallrock sulfidation reactions, while lesser gold may have been precipitated in rare quartz-sulfide veinlets by boiling.

Newton is thought to be typical of deep intermediate-sulfidation-style gold deposits related to the shallow parts of porphyry systems, and there is some evidence in the presence of rare hypersaline fluid inclusions and localized potassic alteration for the presence of such a system at depth, although this has not been explored to date.

Acknowledgements

This work was funded by a Strategic Projects Grant from the Natural Sciences and Engineering Research Council of Canada (STPGP413264-11) and industry partners Amarc Resources Ltd., Geotech Ltd., Gerald G. Carlson, and John A. Chapman. Amarc Resources Ltd. is thanked for providing access to drill cores of the Newton property. We thank Diane Nicolson for her support on the Newton deposit, and Ben Harding for field assistance. We also thank Martin von Dollen, Diane Caird, Andy DuFrane, Robert Dokken, and Robert Creaser for their help with sample preparation, XRD analysis, zircon U-Pb dating, and molybdenite Re-Os dating, respectively.

References

Albinson, T., Norman, D.I., Cole, D., and Chomiak, B. 2001. Controls on formation of low-sulfidation epithermal deposits in Mexico: Constraints from fluid inclusion and stable isotope data. Society of Economic Geology Special Publication, 8: 1–32.

Andrew, K.P.E. 1988. Geology and genesis of the Wolf precious metal epithermal prospect and the Capoose base and precious metal porphyry-style prospect, Capoose Lake area, central British Columbia. MSc. thesis, University of British Columbia, Vancouver, B.C.

Atwater, T. 1989. Plate tectonic history of the northeast Pacific and western North

America. In The eastern Pacific Ocean and Hawaii: Boulder, Colorado. Edited by Winterer, E.L., Hussong, D.M., and Decker, R.W. Geological Society of America. Geology of North America, N: 21–72.

Bevier, M.L. 1983. Implications of Chemical and Isotopic Composition for Petrogenesis of Chilcotin Group Basalts, British Columbia. Journal of Petrology, 24: 207–226.

Bevier, M.L. 1983. Regional stratigraphy and age of Chilcotin Group basalts, south-central British Columbia. Canadian Journal of Earth Sciences, 20: 515–524.

Briqueu, L., Bougault, H., Joron, J.L. 1984. Quantification of Nb, Ta, Ti and V anomalies in magmas associated with subduction zones: petrogenetic implications. Earth and Planetary Science Letters, 68: 297–308.

Brown, G.G., Thorpe, R.S., and Webb, P.C. 1984, The geochemical characteristics of granitoids in contrasting arcs and comments on magma sources. Journal of the Geological Society, 141: 413–426.

Bodnar, R.J., Burnham, C.W., and Sterner, S.M. 1985, Synthetic fluid inclusions in natural quartz. III. Determination of phase equilibrium properties in the system H_2O-NaCl to 1000°C and 1500 bars. Geochimica et Cosmochimica Acta, 49: 1861-1873.

Bodnar, R.J. 1993. Revised equation and table for determining the freezing point depression of H_2O-NaCl solutions. Geochimica et Cosmochimica Acta, 57, 683–684.

Bodnar, R.J., and Vityk, M.O. 1994. Interpretation of microthermometric data for H_2O-NaCl fluid inclusions. In Fluid inclusions in minerals: Methods and applications. Edited by B. DeVivo and M.L. Frezzotti. Virginia Tech Press, Blacksburg, VA. pp. 117–130.

Bordet, E., Hart, C, and McClenaghan, L. 2011. Epithermal-style Au-Ag mineralization in Cretaceous to Eocene felsic volcanic complexes, central British Columbia, western Canada. In Let's Talk Ore Deposits Proceedings of the Eleventh Biennial SGA Meeting. Edited by F. Barra, M. Reich, E. Campos, F. Tornos. Ediciones Universidad Catolica del Norte, Antofagasta, Chile. pp. 714–716.

Bozzo, A.T., Chen, H.S., Kass, J.R., and Barduhn, A.J. 1975. The properties of the hydrates of chlorine and carbon dioxide. Desalination, 16: 303–320.

Buchanan, L.J. 2000. The geology of the San Cristobal deposit. Abstracts with Programs - Society of Mining Engineers: 60.

Candela, P.A. 1992. Controls on ore metal ratios in granite-related ore systems: An experimental and computational approach. Transactions of the Royal Society of Edinburgh, Earth Sciences, 83: 317–326.

Chang, Z., Hedenquist, J.W., White, N.C., Cooke, D.R., Roach, M. 2011. Exploration Tools for Linked Porphyry and Epithermal Deposits: Example from the Mankayan Intrusion-Centered Cu-Au District, Luzon, Philippines. Economic Geology, 106: 1365–1398.

Christie, G., Lipiec, I.T., Simpson, R.G., Horton, J., Borntraeger, B. 2014. Technical report on feasibility study of the Blackwater Gold deposit, British Columbia. New Gold Inc. NI43–101 Report.

Colpron, M., and Price, R.A. 1995. Tectonic significance of the Kootenay terrane, southeastern Canadian Cordillera: An alternative model. Geology, 23: 25–28.

Colpron, M., Nelson, J.L. and Murphy, D.C. 2006. A tectonostratigraphic framework for the pericratonic terranes of the northern Canadian Cordillera. In Paleozoic Evolution and Metallogeny of Pericratonic Terranes at the Ancient Pacific

Margin of North America, Canadian and Alaskan Cordillera. Edited by M. Colpron and J.L. Nelson. Geological Association of Canada Special Paper 45. pp. 1–23.

Cooke, D.R., McPhail, D.C., and Bloom, M.S. 1996. Epithermal gold mineralization, Acupan, Baguio district, Philippines: Geology, mineralization, alteration, and the thermochemical environment of ore deposition. Economic Geology, 91: 243–272.

Cooke, D.R., Deyell, C.L., Waters, P.J., Gonzales, R.I., and Zaw, K. 2011. Evidence for Magmatic-Hydrothermal Fluids and Ore-Forming Processes in Epithermal and Porphyry Deposits of the Baguio District, Philippines. Economic Geology, 106: 1399–1424.

Diamond, L.W. 1992. Stability of CO_2 clathrate hydrate + CO, liquid + CO_2 vapour + aqueous KCI-NaCl solutions: Experimental determination and application to salinity estimates of fluid inclusions. Geochimica et Cosmochimica Acta, 56: 273–280.

Edwards, B.R., and Russell, J.K. 1999. Northern Cordilleran volcanic province: A northern Basin and Range. Geology, 27: 243–246.

Edwards, B.R., and Russell, J.K. 2000. Distribution, nature, and origin of Neogene-Quaternary magmatism in the northern Cordilleran volcanic province, Canada. GAS bulletin, 112: 1280–1295.

Einaudi, M.T., Hedenquist, J.W., and Inan, E. 2003. Sulfidation state of hydrothermal fluids: The porphyry-epithermal transition and beyond. Society of Economic Geologists Special Publication 10. pp. 285−313.

Engebretson, D.C., Cox, Allan, and Gordon, R.G. 1985. Relative motions between oceanic and continental plates in the Pacific Basin. Geological Society of

America, Special Paper 206, pp. 59.

English, J.M., and Johnston, S.T. 2004. The Laramide Orogeny: What were the Driving Forces? International Geology Review, 46: 833–838.

Friedman, R., Diakow, L., Lane, R., and Mortensen, J. 2001. New U Pb age constraints on latest Cretaceous magmatism and associated mineralization in the Fawnie Range, Nechako Plateau, central British Columbia. Canadian Journal of Earth Sciences, 38: 619–637.

Gabrielse, H. 1991. Late Paleozoic and Mesozoic terrane interactions in north-central British Columbia. Canadian Journal of Earth Sciences, 28: 947–957.

Gabrielse, H., and Yorath, C.J. 1991. The Cordilleran orogen in Canada. Geoscience Canada, 16: 67–83.

Gabrielse, H., Murphy, D.C., and Mortensen, J.K. 2006. Cretaceous and Cenozoic dextral orogen-parallel displacements, magmatism and paleogeography, north-central Canadian Cordillera. In Paleogeography of the North American Cordillera: Evidence For and Against Large-Scale Displacements. Edited by J.W. Haggart, J.W.H. Monger, and R.J. Enkin. Geological Association of Canada, Special Paper 46, pp. 255–276.

Gill, J.B. 1981. Orogenic andesites and plate tectonics. New York, Springer-Verlag, pp. 390.

Gillespie, J.M., and Heller, P.L. 1995. Beginning of foreland subsidence in the Columbian-Sevier belts, southern Canada and northwest Montana. Geology, 23: 723–726.

Goldstein, R.H. 2003. Petrographic analysis of fluid inclusions. *In* Fluid inclusions: Analysis and interpretation. *Edited by* I. Samson, A. Anderson, and D. Marshall. Mineralogical Association of Canada, Short Course Handbook, 32: 9–53.

Goldstein, R.H., and Reynolds, T.J. 1994. Systematics of fluid inclusions in diagenetic minerals. Society of Economic Paleontologists and Mineralogists, Short Course Handbook 31, p. 199.

Green, T.H., and Pearson, N.J. 1985. Experimental determination of REE partition coefficients between amphibole and basaltic to andesitic liquids at high pressure. Geochimica et Cosmochimica Acta, 49: 1465–1468.

Gromet, L.P., Silver, L.T. 1983. Rare earth element distributions among minerals in a granodiorite and their petrogenetic implications. Geochimica et Cosmochimica Acta, 47: 925–939.

Haas, J.L. 1971. The effect of salinity on the maximum thermal gradient of a hydrothermal system at hydrostatic pressure. Economic Geology, 66: 940–946.

Hanson, G. 1980. Rare earth elements in petrogenetic studies of igneous systems. Annual Review of Earth and Planetary Sciences, 8: 371–406.

Harms, T. A. 1986. Structural and tectonic analysis of the Sylvester Allochthon, SW McDame map area, northern British Columbia: Implications for paleogeography and accretion. Ph.D. thesis, University of Arizona, Tucson, America.

Hedenquist, J.W., Arribas, A., Gonzalez-Urien, E. 2000. Exploration for epithermal gold deposits. Reviews in Economic Geology, 13: 245–277.

Hoskin, P.W.O. 2000. Patterns of chaos: Fractal statistics and the oscillatory chemistry of zircon. Geochimica et Cosmochimica Acta, 64: 1905–1923.

Hübert, J., Lee, B.M., Liu, L., Unsworth, M.J., Richards, J.P., Abbassi, B., Cheng, L.Z., Oldenburg, D.W., Legault, J.M., Rebagliati, M. Three-dimensional imaging of a Ag-Au-rich epithermal system in British Columbia, Canada using airborne ZTEM and ground-based magnetotelluric data. Geophysics, in press.

Lamb, S., Hoke, L., Kennan, L., and Dewey, J. 1997. Cenozoic evolution of the Central Andes in Bolivia and northern Chile. Geological Society [London] Special Publication 121, pp. 237–264.

Lane, R.A., and Schroeter, T.G. 1997. A review of metallic mineralization in the Interior Plateau, central British Columbia. In Interior Plateau Geoscience Project, Summary of Geological, Geochemical and Geophysical Studies. Edited by L.J. Diakow, and J.M. Newell. BCGS Survey Branch Open File 1996-2, pp. 237–256.

Lepitre, M.E., Mortensen, J.K. Friedman, R.M., and Jordan, S.J. 1998. Geology and U-Pb geochronology of intrusive rocks associated with mineralization in the northern Tahtsa Lake district, west-central British Columbia. Geological Fieldwork 1997, British Columbia Ministry of Energy and Mines, Paper 1998-1, pp. 1–32.

Ludwig, K.R. 2003. Isoplot/Ex, a geochronological toolkit for Microsoft Excel, Version 3.00. Berkeley Geochronology Center, Special Publication 4, pp. 1–43.

Lynch, G. 1995. Geochemical polarity of the Early Cretaceous Gambier Group, southern Coast Belt, British Columbia. Canadian Journal of Earth Sciences, 32: 675–685.

MacIntyre, D.G., Ash, C., and Britton, J. 1994. Geological compilation, Skeena-Nass area, west-central British Columbia, NTS 93E, L, M; 94D; 103G, H, I, J, P; 104A, B. British Columbia Ministry of Energy, Mines and Petroleum Resources, Open File 1994–14.

Massey, N.W.D., MacIntyre, D.G., Desjardins, P.J., and Cooney, R.T. 2005. Digital geology map of British Columbia; whole province. British Columbia Ministry of Energy, Mines and Petroleum Resources, Open-File 2005–01.

McClenaghan, L. 2013. Geology and Genesis of the Newton Bulk-Tonnage Gold-Silver Deposit, Central British Columbia. M.Sc. thesis, The University of British Columbia, Vancouver, B.C.

McLaren, G., and Rouse, J. 1989. Geology and Geochemistry of the Taseko Lakes Area (NTS 092O/3, 4, 5, 6). British Columbia Ministry of Energy, Mines and Petroleum Resources, Open File 1989–25.

McMillan, W.J., Thompson, J.F.H., Hart, C.J.R., and Johnston, S.T. 1995. Regional geological and tectonic setting of porphyry deposits in British Columbia and Yukon Territory. In Porphyry deposits of the northwestern Cordillera of North America. Edited by T.G. Schroeter. Canadian Institute of Mining, Metallurgy and Petroleum, Special Volume 46, pp. 40–57.

Middlemost, E.A.K. 1994. Naming materials in the magma/igneous rock system. Earth-Science Reviews, 37: 215–224.

Mihalasky, M.J., Bookstrom, A.A., Frost, T.P., and Ludington, S. 2011. Porphyry Copper Assessment of British Columbia and Yukon Territory, Canada. U.S. Geological Survey Scientific Investigations Report 2010-5090-C.

Mikucki, J.E. 1998. Hydrothermal transport and depositional processes in Archean lode–gold systems: A review. Ore Geology Review, 13: 307–321.

Monger, J., and Price, R. 2002. The Canadian Cordillera: Geology and Tectonic Evolution. CSEG Recorder, 2: 17–36.

Nelson, J., and Colpron, M. 2007. Tectonics and metallogeny of the British Columbia, Yukon and Alaskan Cordillera, 1.8 Ga to the present. In Mineral Deposits of Canada: A Synthesis of Major Deposit-Types, District Metallogeny, the Evolution of Geological Provinces, and Exploration Methods. Edited by W.D. Goodfellow. Geological Association of Canada, Mineral Deposits Division, Special Publication 5, pp. 755–791.

Naney, M.T. 1983. Phase equilibria of rock-forming ferromagnesian silicates in granitic systems. American Journal of Science, 283: 993–1033.

Noble, D.C., Eyzaguirre, V.R., and McKee, E.H. 1990. Precious-metal mineralization of Cenozoic age in the Andes of Peru. Circum-Pacific Council for Energy and Mineral Resources, Earth-Science Series, 11: 207–212.

Nokleberg, W.J., Parfenov, L.M., Monger, J. W. H., Norton, I.O., Khanchun, A.I., Stone, D.B., Scotese, C.R., Scholl, D.W., and Fujita, K. 2000. Phanerozoic Tectonic Evolution of the Circum-North Pacific. U.S. Geological survey Professional Paper 1626, p. 122 .

Nokleberg, W.J., Bundtzen, T., Eremin, R.A., Ratkin, V.V., Dawson, K.M., Shpikerman, V.V., Goryachev, N.A., Byalobzhesky, S.G., Frolov, Y.F., Khanchuck, A.I., Koch, R.D., Monger, J.W.H., Pozdeev, A.A., Rozenblum, I.S., Rodionov, S.M., Parfenov, L.M., Scotese, C.R. and Sidorov, A.A. 2005. Metallogenesis and tectonics of the Russian Far East, Alaska and the Canadian Cordillera. U.S. Geological Survey Professional Paper 1697, p. 397.

Parrish, R.R., Carr, S.D., and Parkinson, D.L. 1988. Eocene extensional tectonics and geochronology of the southern Omineca Belt, British Columbia and Washington. Tectonics, 7: 181–212.

Pearce, J.A., Harris, N.B.W., and Tindle, A.G. 1984. Trace element discrimination diagrams for the tectonic interpretation of granitic rocks. Journal of Petrology, 25: 956-983.

Peccerillo, A., and Taylor, S.R. 1976. Geochemistry of Eocene calc-alkaline volcanic rocks from the Kastamonu area, northern Turkey. Contributions to Mineralogy and Petrology, 58: 63–81.

Pressacco, R. 2012. Technical report on the initial mineral resource estimate for the newton project, central British Columbia, Canada. Amarc Resources Ltd. NI43–101 report.

Richards, J.P. 2003. Tectono-magmatic precursors for porphyry Cu-(Mo-Au) deposit formation. Economic Geology, 98: 1515–1533.

Riddell, J. M. 2006. Geology of the Southern Nechako Basin NTS 92N, 92O, 93B, 93C, 93F, 93G. British Columbia Ministry of Energy, Mines and Petroleum Resources, Open-File 2006–01.

Riddell, J. 2011. Lithostratigraphic and tectonic framework of Jurassic and Cretaceous Intermontane sedimentary basins of south-central British Columbia. Canadian Journal of Earth Sciences, 48: 870–896.

Roback, R. C., Sevigny, J. H., Walker, N. W. 1994. Tectonic setting of the Slide Mountain terrane, southern British Columbia. Tectonics, 13: 1242–1258.

Roedder, E., and Bodnar, R.J. 1980. Geologic pressure determinations from fluid inclusion studies. Annual Review of Earth and Planetary Sciences, 8: 263–301.

Roedder, E. 1984. Fluid inclusions. Reviews in Mineralogy, 12, p. 644.

Rollinson, H. 1993. Using Geochemical Data. Evaluation, Presentation, Interpretation, p. 352.

Seward, T.M. 1989. The hydrothermal chemistry of gold and its implications for ore formation: Boiling and conductive cooling as examples. In The Geology of Gold Deposits. Edited by R.R. Keays, W.R.H. Ramsay, D.I. Groves. The Perspective in 1988, Economic Geology Monograph Series, 6: 398–404.

Seward, T.M. 1991. The hydrothermal geochemistry of gold. In Gold Metallogeny and Exploration. Edited by R.P. Foster, pp. 37–62.

Sillitoe, R.H., and Hedenquist, J.W. 2003. Linkages between volcanotectonic settings, ore-fluid compositions, and epithermal precious-metal deposits. Society of Economic Geologists Special Publication 10, pp. 315−343.

Sisson, T.W. 1994. Hornblende-melt trace-element partitioning measured by ion microprobe. Chemical Geology, 117: 331–344.

Simonetti, A., Heaman, L.M., Hartlaub, R.P., Creaser, R.A., MacHattie, T.G., and Bohn, C. 2005. U–Pb zircon dating by laser ablation-MC-ICP-MS using a new multiple ion counting Faraday collector array. Journal of Analytical Atomic Spectrometry, 20: 677–686.

Steele-MacInnis, M., Lecumberri-Sanchez, P., and Bodnar, R.J. 2012. HOKIEFLINCS_H2O-NACL: A Microsoft Excel spreadsheet for interpreting microthermometric data from fluid inclusions based on the PVTX properties of H2O–NaCl. Computers & Geosciences, 49: 334–337

Sterner, S.M., Hall, D.L., and Bodnar, R.J. 1988. Synthetic fluid inclusions. V. Solubility relations in the system NaCl-KCl-H_2O under vapor-saturated conditions. Geochimica et Cosmochimica Acta, 52: 989–1005.

Stock, J., and Molnar, P. 1988. Uncertainties and implications of the Late Cretaceous and Tertiary position of North America relative to the Farallon, Kula, and Pacific plates. Tectonics, 7: 1339–1384.

Sun, S.S., and McDonough, W.F. 1989. Chemical and isotopic systematics of oceanic basalts: Implications for mantle composition and processes. Geological Society of London Special Publication, 42: 313–345.

Tera, F., and Wasserburg, G.J. 1972. U-Th-Pb systematics in three Apollo 14 basalts and the problem of initial Pb in lunar rocks. Earth and Planetary Science Letters, 14: 281–304.

Umhoefer, P.J. and Schiarizza, P. 1996. Latest Cretaceous to early Tertiary dextral strike-slip faulting on the southeastern Yalakom fault system, southeastern Coast belt, British Columbia. Geological Society of America Bulletin, 108: 768–785.

Wheeler, J.O., Brookfield, A.J., Gabrielse, H., Monger, J.W.H., Tipper, H.W. and Woodsworth, G.J. 1991. Terrane map of the Canadian Cordillera: Geological Survey of Canada, Map 1713A, scale 1: 2 000000.

Figure captions

Fig. 1. Terrane map of the British Columbian Cordillera, showing the location of the Newton Au deposit in the southern Stikinia terrane. Fault abbreviations: FF-Fraser fault; YF-Yalakom fault. Modified from Nelson and Colpron (2007).

Fig. 2. Geological map of the British Columbian Cordillera, showing major terranes, Cretaceous to Eocene volcanic and intrusive rocks, regional faults, and Late Cretaceous-Eocene epithermal gold deposits in the Newton area. Epithermal deposit abbreviations: B-Blackwater; BD-Black Dome; C-Capoose; Cl-Clisbako; W-Wolf. Redrawn from Pressacco (2012).

Fig. 3. Regional geological map of the Newton area and its surroundings. Modified from Massey et al. (2005).

Fig. 4. Geological map of the Newton property. Modified from McClenaghan (2013).

Fig. 5. Hand specimens of the main lithological units in the Newton deposit: (A) chlorite-epidote-altered diorite (NT067); (B) biotite-altered diorite (NT089); (C) weak propylitic-altered mafic volcanic rock (NT083); (D) quartz-sericite-altered felsic tuff with disseminated pyrite, and pyrite veinlets (NT058); (E) quartz-sericite-altered quartz-feldspar porphyry with disseminated pyrite and a quartz-pyrite veinlet (NT011); (F) quartz-sericite-altered feldspar-quartz-hornblende porphyry with disseminated marcasite, and marcasite veinlets (NT007); (G) kaolinite-altered feldspar-quartz-hornblende porphyry (NT009); (H) sandstone cut by polymetallic veins containing sphalerite, chalcopyrite, arsenopyrite, and carbonate. The carbonate on the surface is

oxidized to an orange color (NT110). The scale divisions are in millimeters.

Fig. 6. Quartz-sericite alteration in the Newton volcanic and intrusive rocks (taken in cross-polarized light): (A) altered felsic volcanic rocks (NT014); (B) altered felsic flow with banded texture (NT002); (C) altered feldspar-quartz-hornblende porphyry (NT038); (D) altered quartz-feldspar porphyry (NT052).

Fig. 7. Alteration in diorite (A and B taken in cross-polarized light; C and D in cross-polarized light): (A) sericite alteration overprinted by later chlorite alteration (NT067); (B) sericite alteration overprinting potassic alteration; plagioclase phenocrysts are replaced by secondary sericite (NT091); (C) propylitic alteration: hornblende phenocrysts are replaced by chlorite (NT135); (D) potassic alteration with secondary biotite (NT091).

Fig. 8. Vein and alteration paragenesis based on hand sample observations and petrographic studies.

Fig. 9. Paragenetic relationships between sulfide minerals (photomicrographs taken in reflected light, except core sample in C): (A) chalcopyrite, sphalerite, and pyrrhotite inclusions in pyrite (quartz-feldspar porphyry; NT011; stage 1 mineralization); (B) electrum inclusions in pyrite (quartz-feldspar porphyry; NT011; stage 1 mineralization); (C) quartz-molybdenite-pyrite vein hosted by quartz-sericite-pyrite-altered felsic volcanic rock (NT060; stage 1 mineralization;); (D) minor sphalerite intergrown with marcasite in felsic volcanic rock (NT028; stage 2 mineralization); (E) chalcopyrite intergrown with sphalerite in felsic volcanic rock (NT028; stage 2

mineralization); (F) polymetallic vein: pyrite, arsenopyrite, chalcopyrite, and sphalerite form a layered sequence in the vein, which is cross-cut by a late calcite vein (felsic volcanic host rock; NT062; stage 3 mineralization). Abbreviations: Apy = arsenopyrite, Cpy = chalcopyrite, Mo = molybdenite, Mrc = marcasite, Po = pyrrhotite, Py = pyrite, Sp = sphalerite.

Fig. 10. Total alkali (Na_2O+K_2O) versus silica diagram (Middlemost 1994) showing the compositions of igneous rocks from the Newton area. The felsic volcanic rock and quartz-feldspar porphyry data are from McClenaghan (2013).

Fig. 11. Harker diagrams showing variations of (A) TiO_2, (B) MgO, (C) P_2O_5, and (D) K_2O versus SiO_2 for igneous rocks from the Newton property. Data for felsic volcanic rocks and quartz-feldspar porphyry are from McClenaghan (2013).

Fig. 12. Tectonic discrimination diagrams for igneous rocks from the Newton property (after Pearce et al. 1984). Abbreviations: syn-COLG = syn-collisional granites, ORG = ocean ridge granites, VAG = volcanic arc granites, WPG = within plate granites.

Fig. 13. Primitive mantle-normalized trace element diagrams for samples of (A) intrusive and (B) extrusive rocks from Newton (primitive mantle normalization values from Sun and McDonough 1989). Data for felsic volcanic rocks and quartz-feldspar porphyry are from McClenaghan (2013).

Fig. 14. C1 Chondrite-normalized REE diagrams for samples of (A) intrusive and (B)

extrusive rocks from Newton (normalization values from Sun and McDonough 1989). Data for felsic volcanic rocks and quartz-feldspar porphyry are from McClenaghan (2013).

Fig. 15. Eu anomaly vs. SiO_2 diagram for samples of igneous rock from Newton ($Eu_n/Eu^* = Eu_n / \sqrt{} Sm_n*Gd_n$).

Fig. 16. Backscattered electron images of typical zircons from the feldspar-quartz-hornblende porphyry (A, NT129) and diorite (B, NT090). Zircons from the diorite are slightly larger than from the feldspar-quartz-hornblende porphyry, and show clear magmatic oscillatory zoning from center to margin. Dark areas are small inclusions of other minerals, which were avoided during analysis.

Fig. 17. U-Pb Tera-Wasserburg diagrams for zircon laser ablation ICPMS data from the feldspar-quartz-hornblende porphyry (A; sample NT129) and diorite (B; sample NT090). The error ellipses are 2 sigma.

Fig. 18. Zircon U-Pb $^{238}U/^{206}Pb$ age histogram and relative probability curve for the diorite sample (NT090).

Fig. 19. Transmitted light photomicrographs showing primary fluid inclusions from stage 1 mineralization: (A) type 1 fluid inclusion assemblage from a quartz-pyrite vein (NT049); (B) type 3 primary multi-phase inclusion (liquid-vapor-halite/opaque mineral) from a quartz-molybdenite-pyrite vein (NT060); (C) type 1 liquid-rich inclusion with type 2 vapor-rich inclusions in a primary fluid inclusion assemblage

from a quartz-pyrite vein (NT049).

Fig. 20. Histograms showing homogenization temperature and salinity distribution for type 1 fluid inclusions from quartz-pyrite (NT049) and quartz-molybdenite-pyrite (NT060) veins.

Fig. 21. Salinity versus homogenization temperature plot for inclusions from quartz-pyrite (NT049) and quartz-molybdenite-pyrite (NT060) veins.

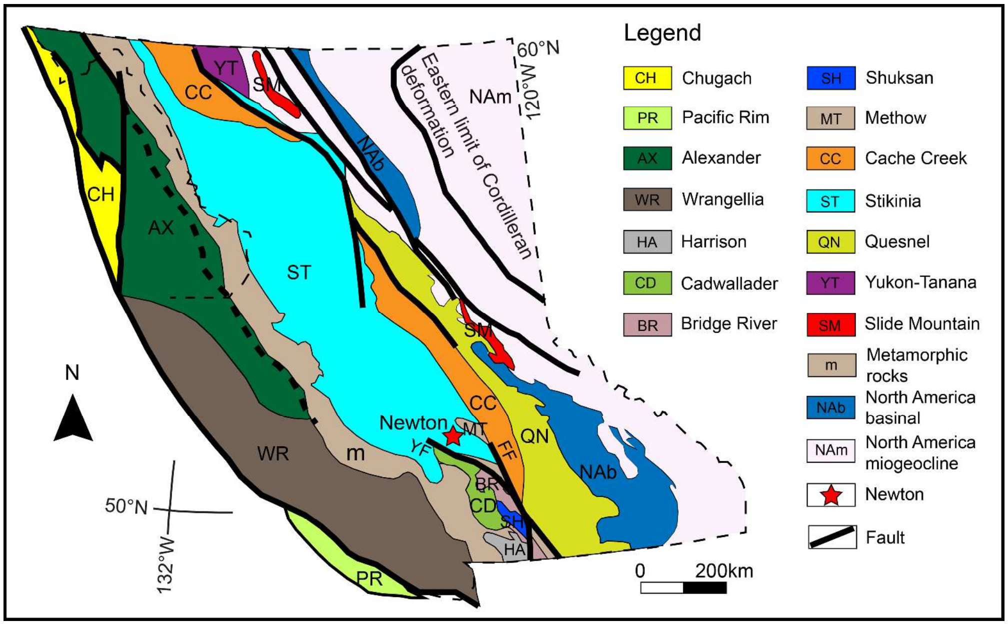

Fig. 1. Terrane map of the British Columbian Cordillera, showing the location of the Newton Au deposit in the southern Stikinia terrane. Fault abbreviations: FF-Fraser fault; YF-Yalakom fault. Modified from Nelson and Colpron (2007).

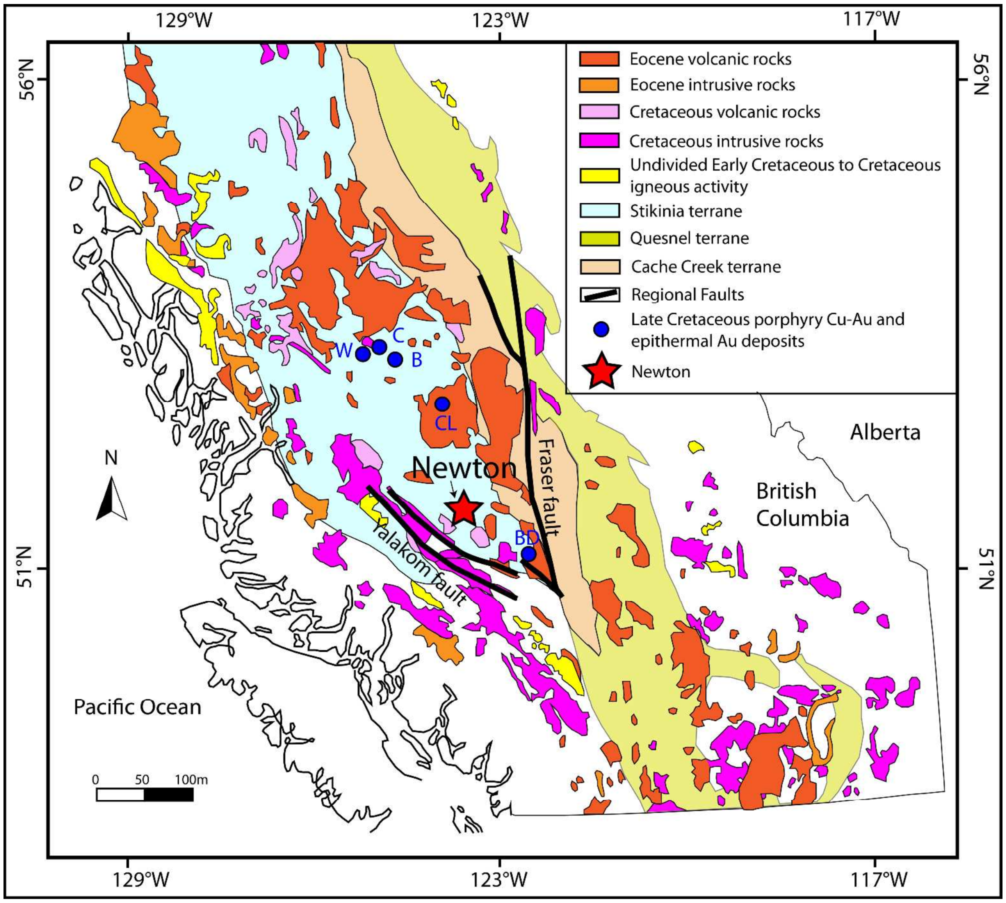

Fig. 2. Geological map of the British Columbian Cordillera, showing major terranes, Cretaceous to Eocene volcanic and intrusive rocks, regional faults, and Late Cretaceous-Eocene epithermal gold deposits in the Newton area. Epithermal deposit abbreviations: B-Blackwater; BD-Black Dome; C-Capoose; Cl-Clisbako; W-Wolf. Redrawn from Pressacco (2012).

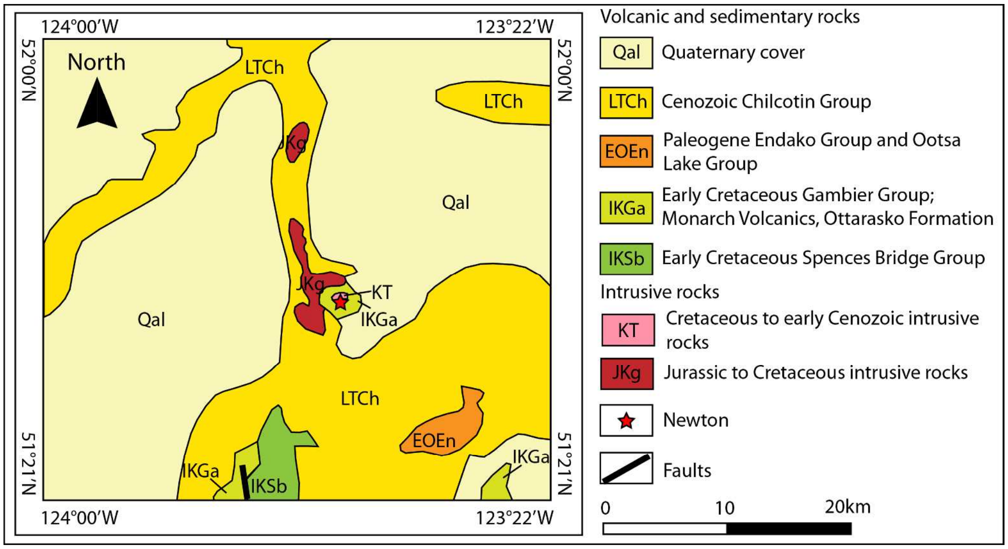

Fig. 3. Regional geological map of the Newton area and its surroundings. Modified from Massey et al. (2005).

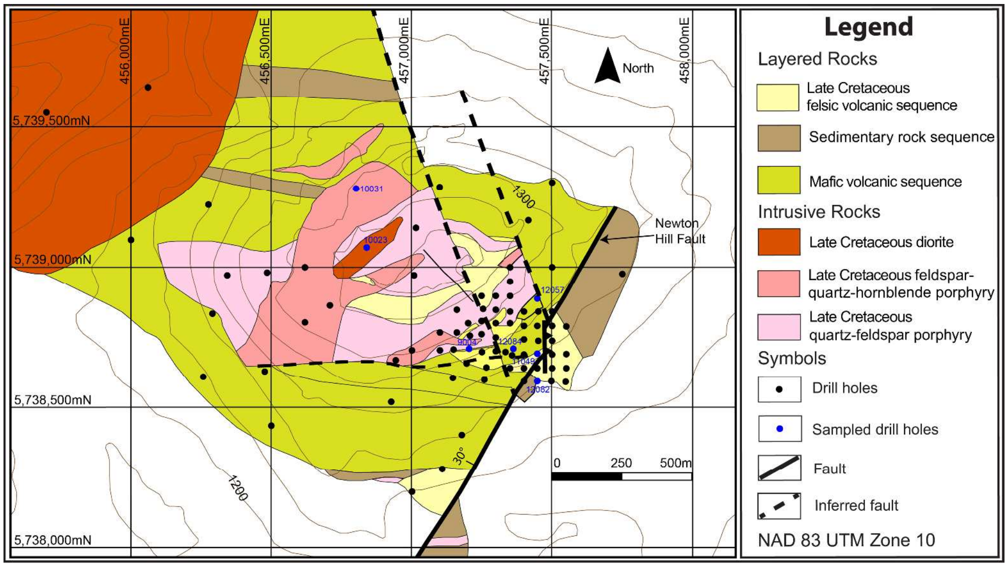

Fig. 4. Geological map of the Newton property. Modified from McClenaghan (2013).

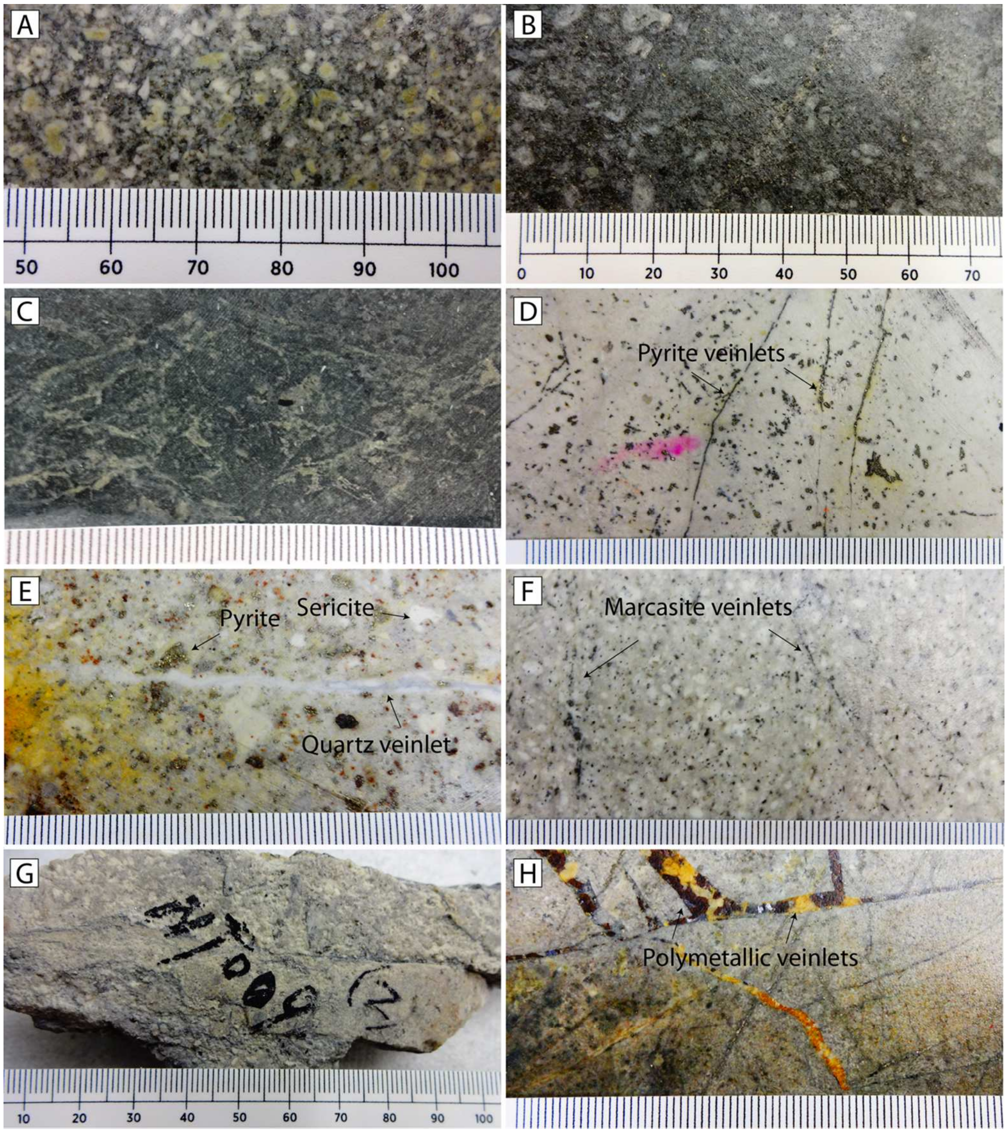

Fig. 5. Hand specimens of the main lithological units in the Newton deposit: (A) chlorite-epidote-altered diorite (NT067); (B) biotite-altered diorite (NT089); (C) weak propylitic-altered mafic volcanic rock (NT083); (D) quartz-sericite-altered felsic tuff with disseminated pyrite, and pyrite veinlets (NT058); (E) quartz-sericite-altered quartz-feldspar porphyry with disseminated pyrite and a quartz-pyrite veinlet (NT011); (F) quartz-sericite-altered feldspar-quartz-hornblende porphyry with disseminated marcasite, and marcasite veinlets (NT007); (G) kaolinite-altered feldspar-quartz-hornblende porphyry (NT009); (H) sandstone cut by polymetallic veins containing sphalerite, chalcopyrite, arsenopyrite, and carbonate. The carbonate on the surface is oxidized to an orange color (NT110). The scale divisions are in millimeters.

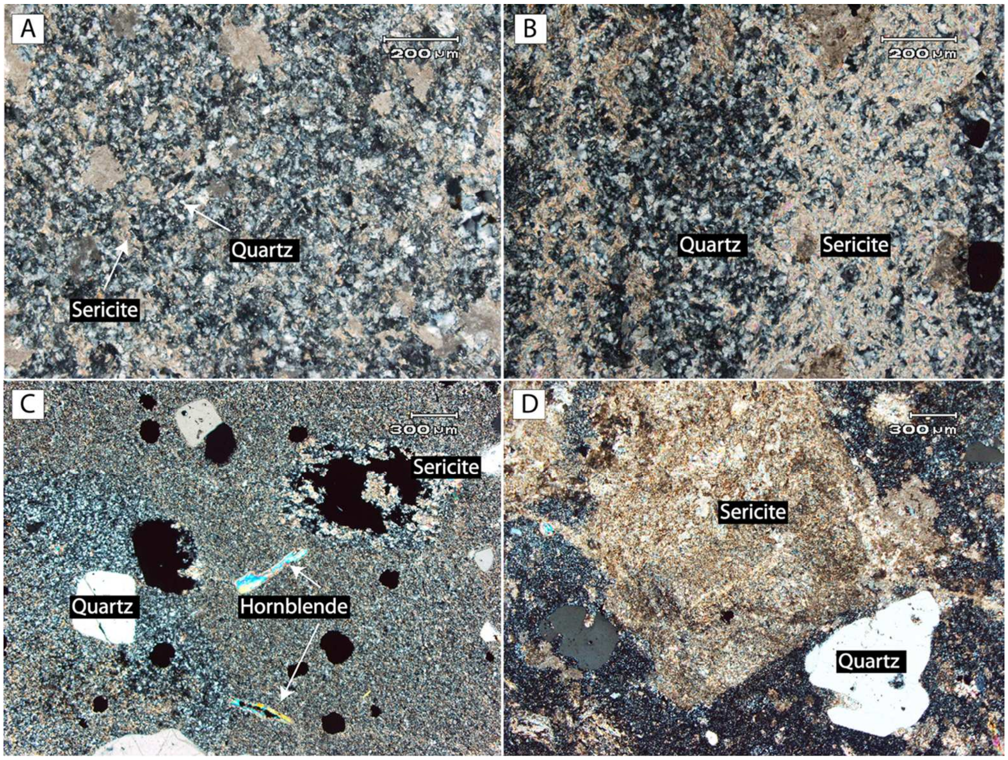

Fig. 6. Quartz-sericite alteration in the Newton volcanic and intrusive rocks (taken in cross-polarized light): (A) altered felsic volcanic rocks (NT014); (B) altered felsic flow with banded texture (NT002); (C) altered feldspar-quartz-hornblende porphyry (NT038); (D) altered quartz-feldspar porphyry (NT052).

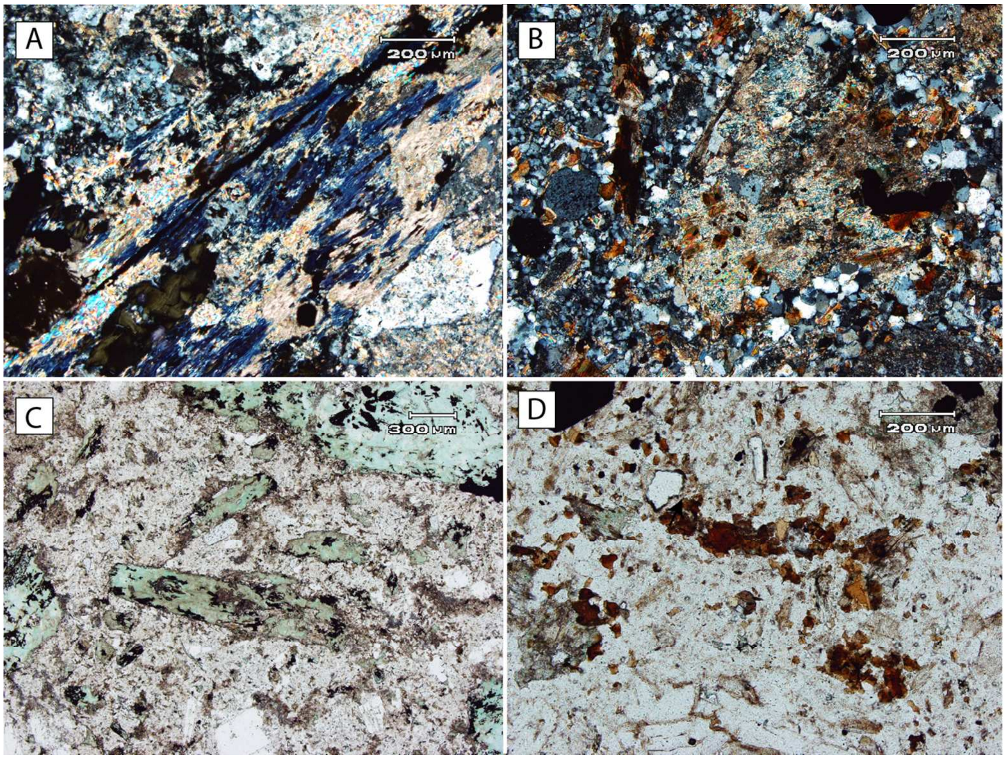

Fig. 7. Alteration in diorite (A and B taken in cross-polarized light; C and D in cross-polarized light): (A) sericite alteration overprinted by later chlorite alteration (NT067); (B) sericite alteration overprinting potassic alteration; plagioclase phenocrysts are replaced by secondary sericite (NT091); (C) propylitic alteration: hornblende phenocrysts are replaced by chlorite (NT135); (D) potassic alteration with secondary biotite (NT091).

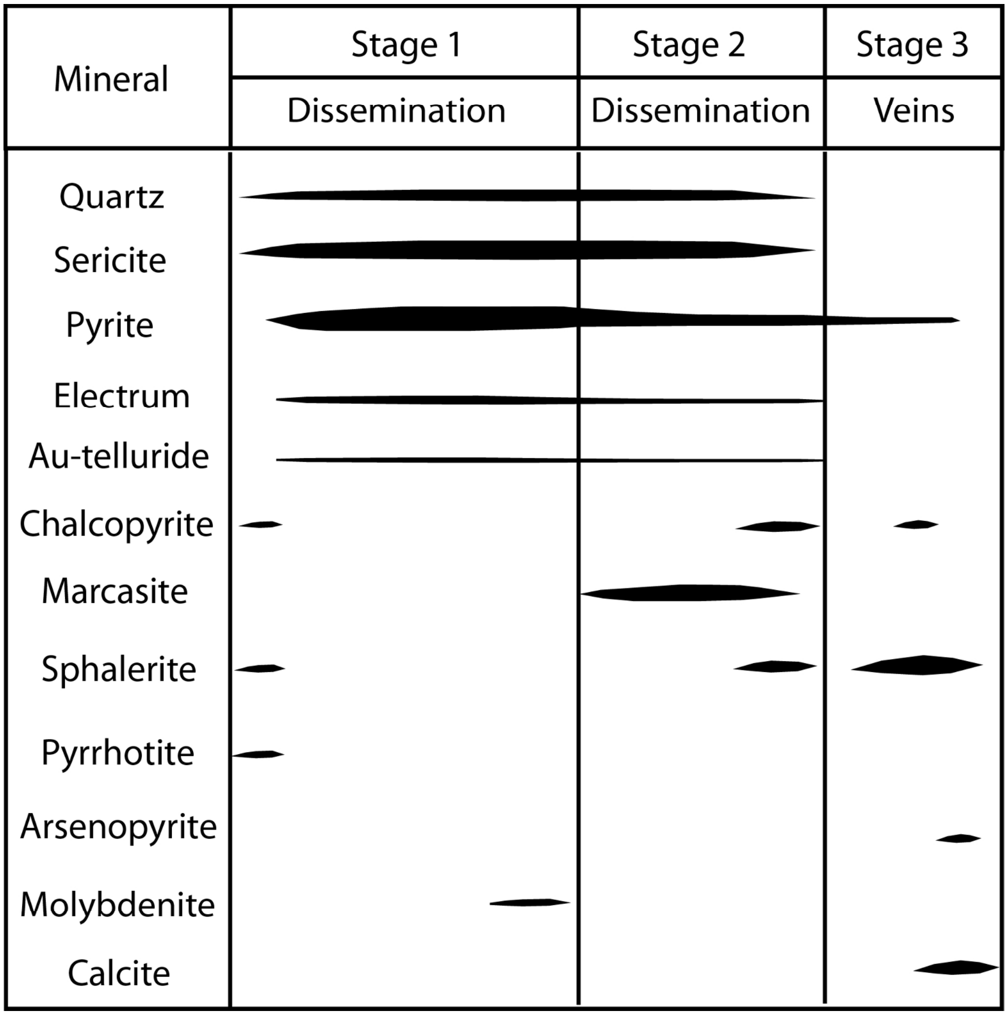

Fig. 8. Vein and alteration paragenesis based on hand sample observations and petrographic studies.

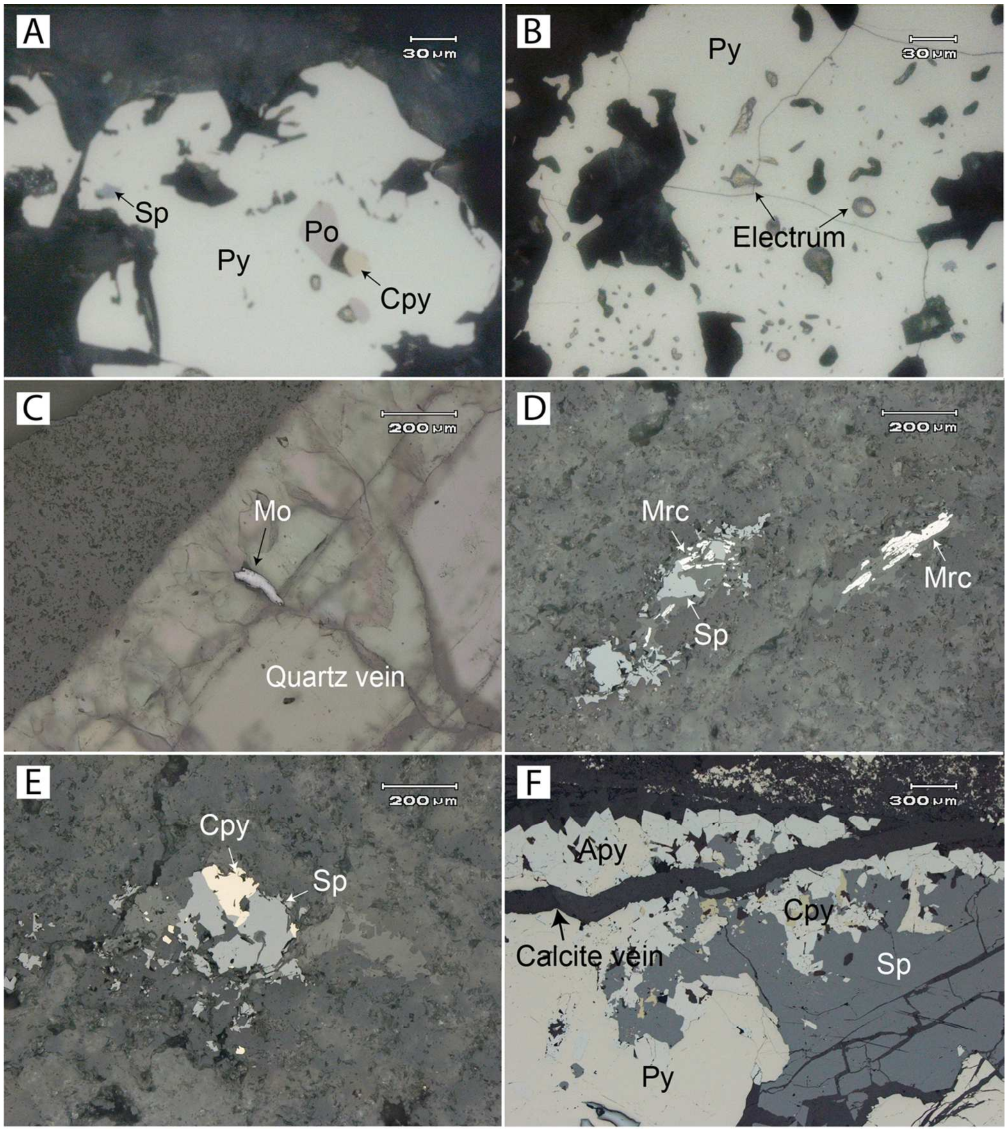

Fig. 9. Paragenetic relationships between sulfide minerals (photomicrographs taken in reflected light, except core sample in C): (A) chalcopyrite, sphalerite, and pyrrhotite inclusions in pyrite (quartz-feldspar porphyry; NT011; stage 1 mineralization); (B) electrum inclusions in pyrite (quartz-feldspar porphyry; NT011; stage 1 mineralization); (C) quartz-molybdenite-pyrite vein hosted by quartz-sericite-pyrite-altered felsic volcanic rock (NT060; stage 1 mineralization;); (D) minor sphalerite intergrown with marcasite in felsic volcanic rock (NT028; stage 2 mineralization); (E) chalcopyrite intergrown with sphalerite in felsic volcanic rock (NT028; stage 2 mineralization); (F) polymetallic vein: pyrite, arsenopyrite, chalcopyrite, and sphalerite form a layered sequence in the vein, which is cross-cut by a late calcite vein (felsic volcanic host rock; NT062; stage 3 mineralization). Abbreviations: Apy = arsenopyrite, Cpy = chalcopyrite, Mo = molybdenite, Mrc = marcasite, Po = pyrrhotite, Py = pyrite, Sp = sphalerite.

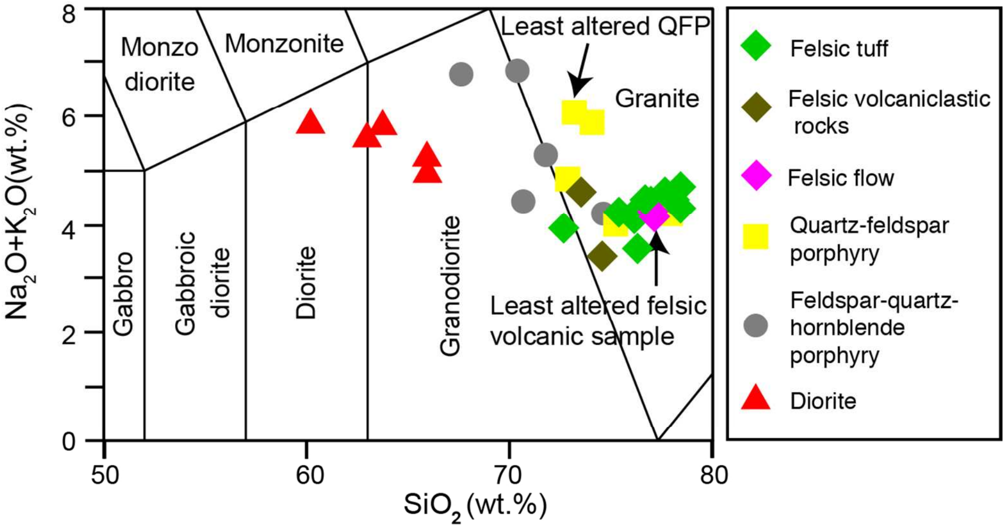

Fig. 10. Total alkali (Na2O+K2O) versus silica diagram (Middlemost, 1994) showing the compositions of igneous rocks from the Newton area. The felsic volcanic rock and quartz-feldspar porphyry data are from McClenaghan (2013).

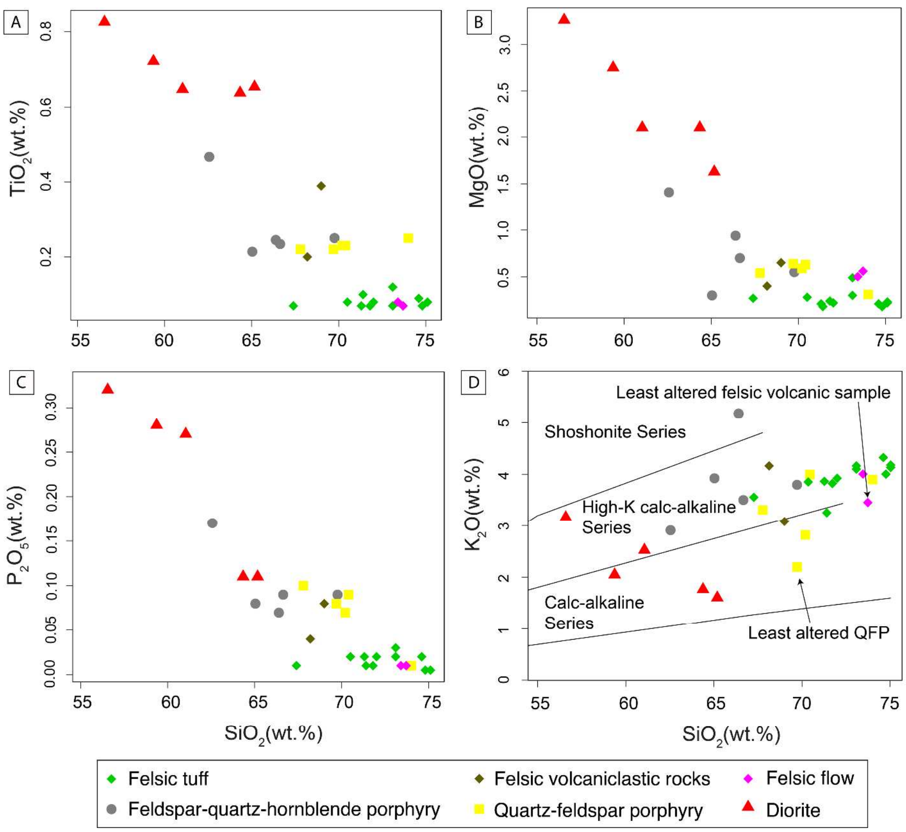

Fig. 11. Harker diagrams showing variations of (A) TiO2, (B) MgO, (C) P2O5, and (D) K2O versus SiO2 for igneous rocks from the Newton property. Data for felsic volcanic rocks and quartz-feldspar porphyry are from McClenaghan (2013).

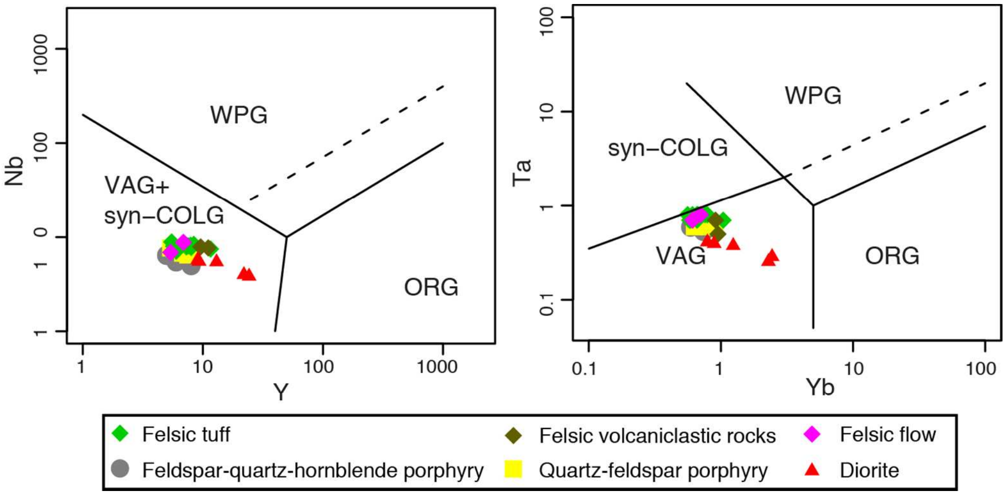

Fig. 12. Tectonic discrimination diagrams for igneous rocks from the Newton property (after Pearce et al., 1984). Abbreviations: syn-COLG = syn-collisional granites, ORG = ocean ridge granites, VAG = volcanic arc granites, WPG = within plate granites.

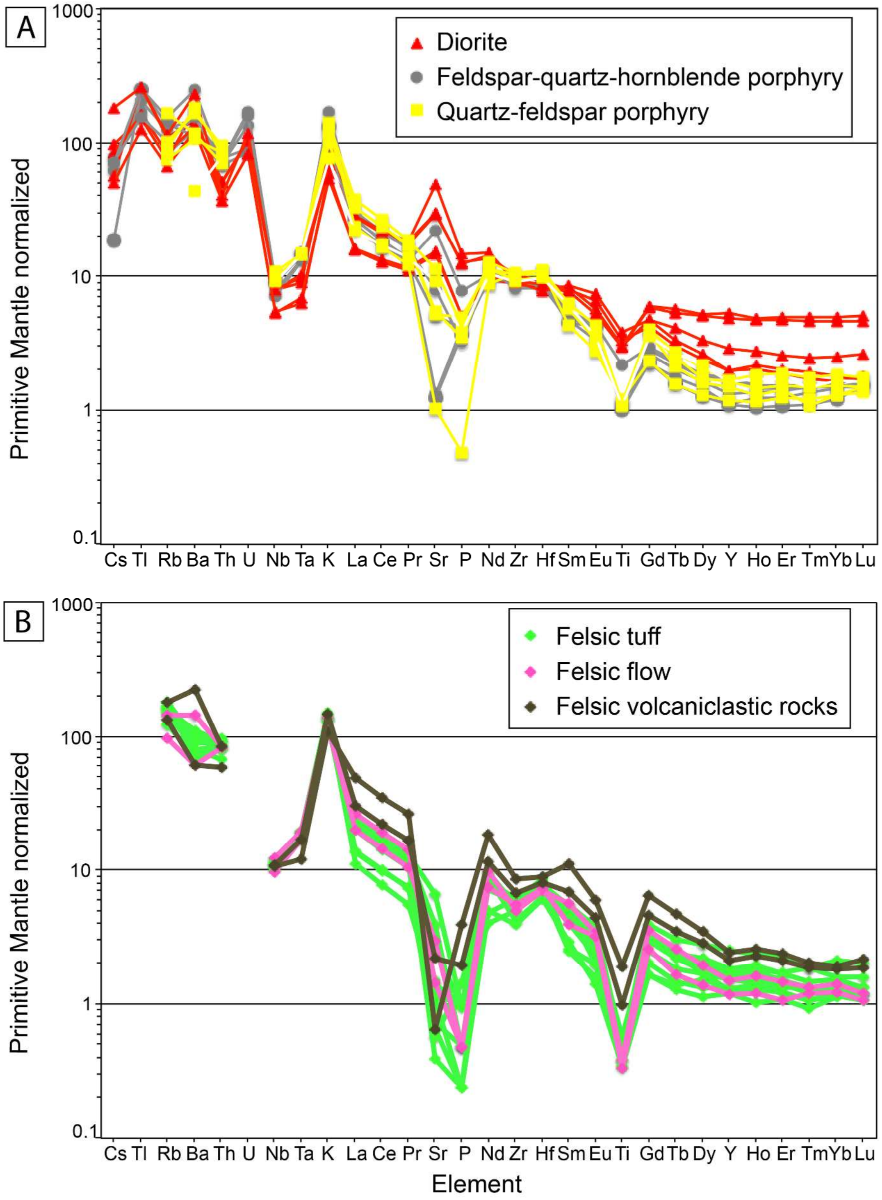

Fig. 13. Primitive mantle-normalized trace element diagrams for samples of (A) intrusive and (B) extrusive rocks from Newton (primitive mantle normalization values from Sun and McDonough, 1989). Data for felsic volcanic rocks and quartz-feldspar porphyry are from McClenaghan (2013).

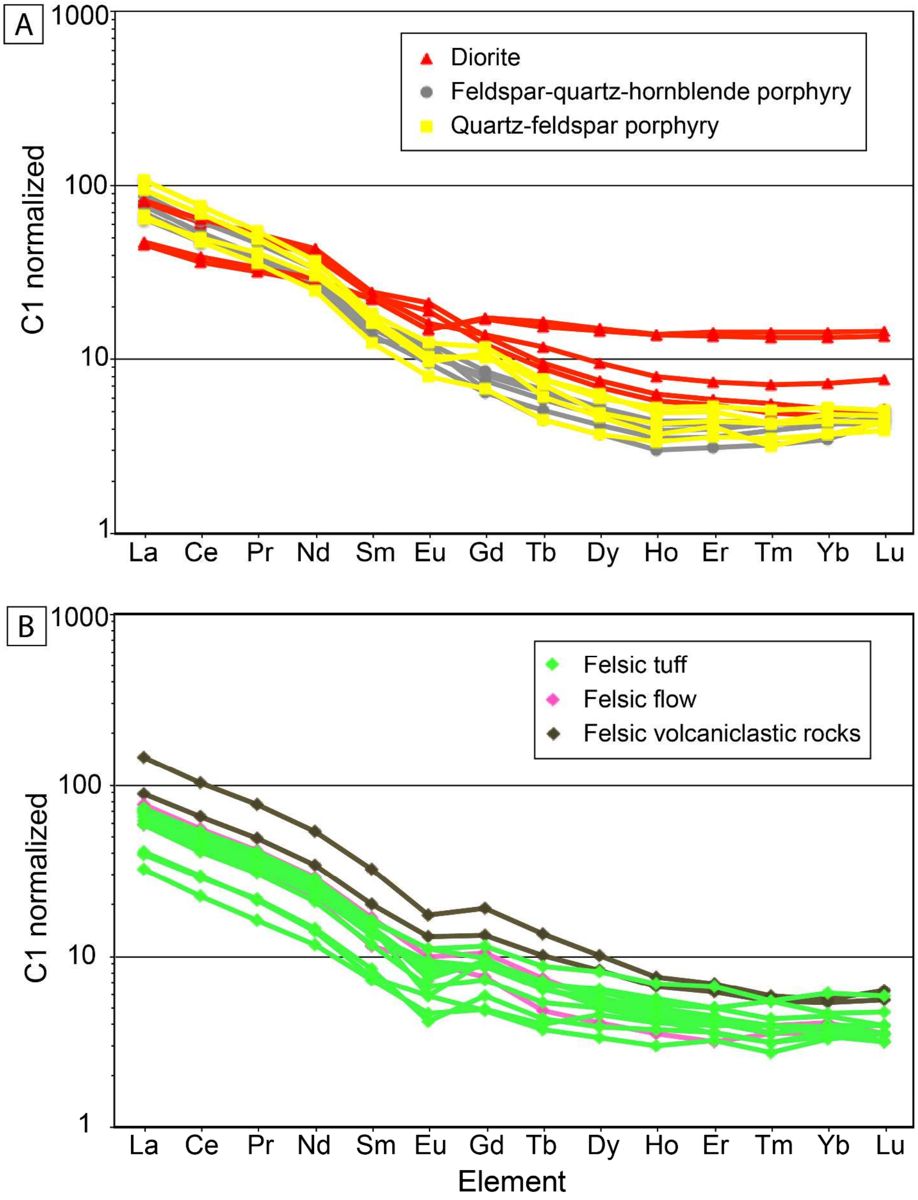

Fig. 14. C1 Chondrite-normalized REE diagrams for samples of (A) intrusive and (B) extrusive rocks from Newton (normalization values from Sun and McDonough, 1989). Data for felsic volcanic rocks and quartz-feldspar porphyry are from McClenaghan (2013).

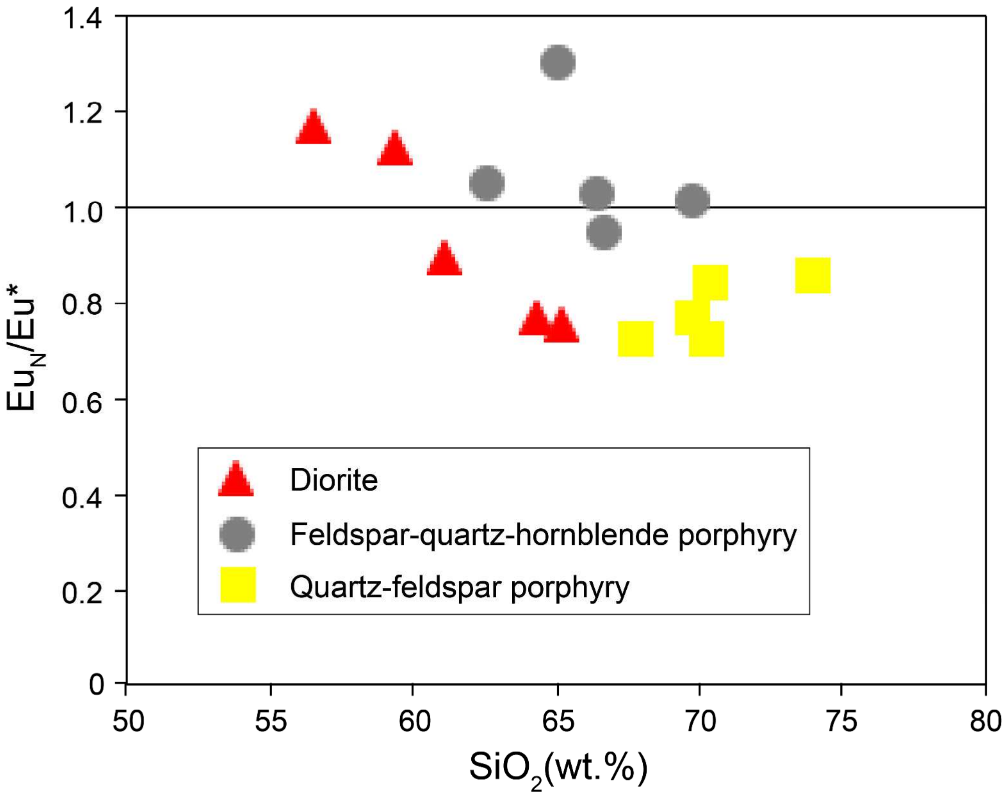

Fig. 15. Eu anomaly vs. SiO2 diagram for samples of igneous rock from Newton (Eun/Eu* = Eun / √ Smn*Gdn).

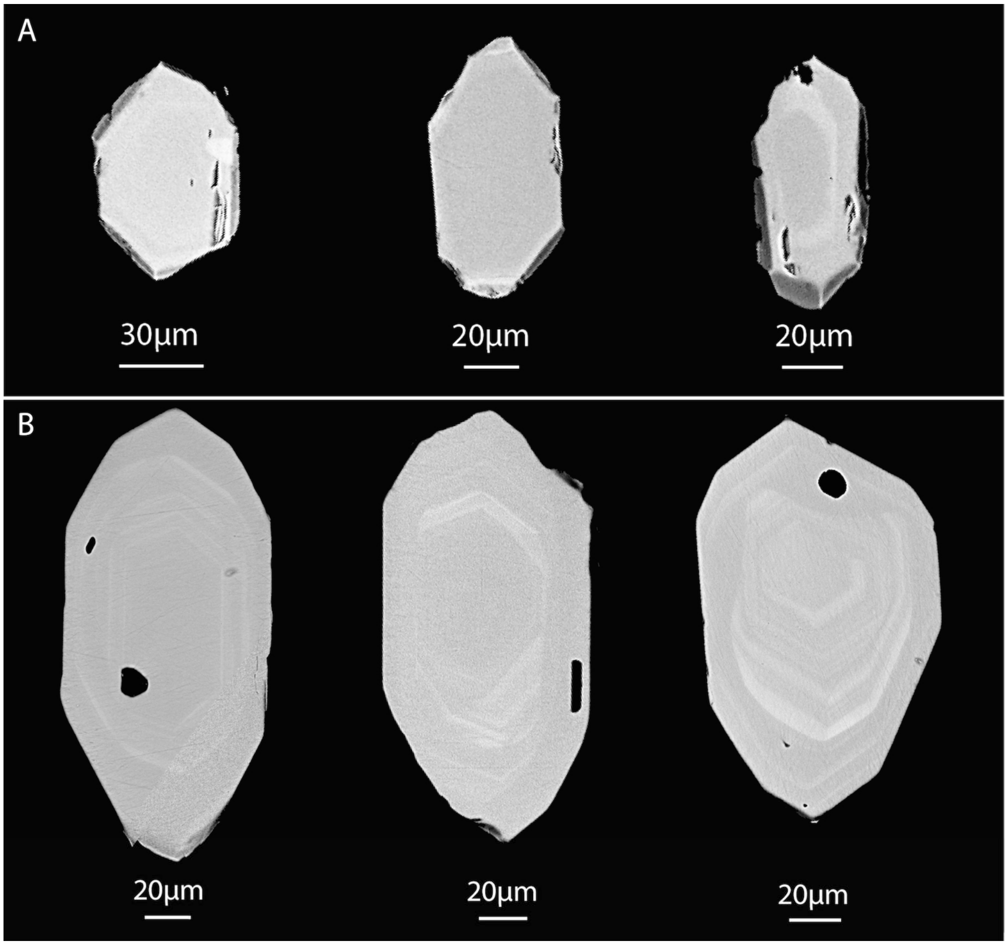

Fig. 16. Backscattered electron images of typical zircons from the feldspar-quartz-hornblende porphyry (A, NT129) and diorite (B, NT090). Zircons from the diorite are slightly larger than from the feldspar-quartz-hornblende porphyry, and show clear magmatic oscillatory zoning from center to margin. Dark areas are small inclusions of other minerals, which were avoided during analysis.

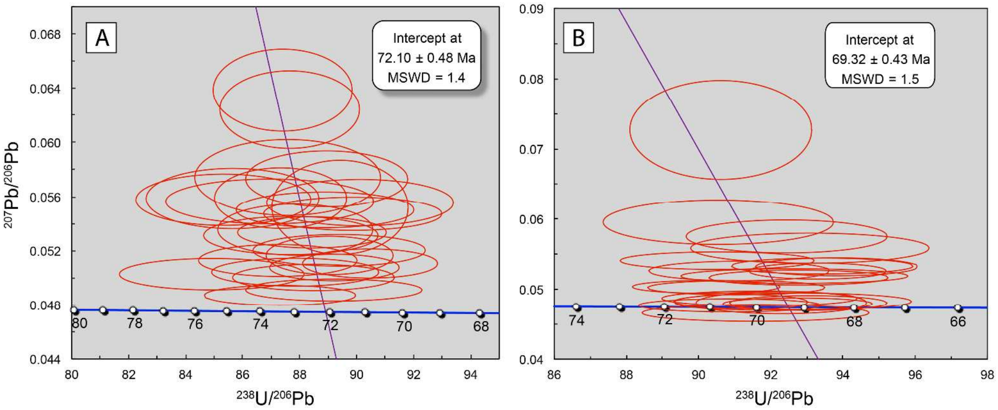

Fig. 17. U-Pb Tera-Wasserburg diagrams for zircon laser ablation ICPMS data from the feldspar-quartz-hornblende porphyry (A; sample NT129) and diorite (B; sample NT090). The error ellipses are 2 sigma.

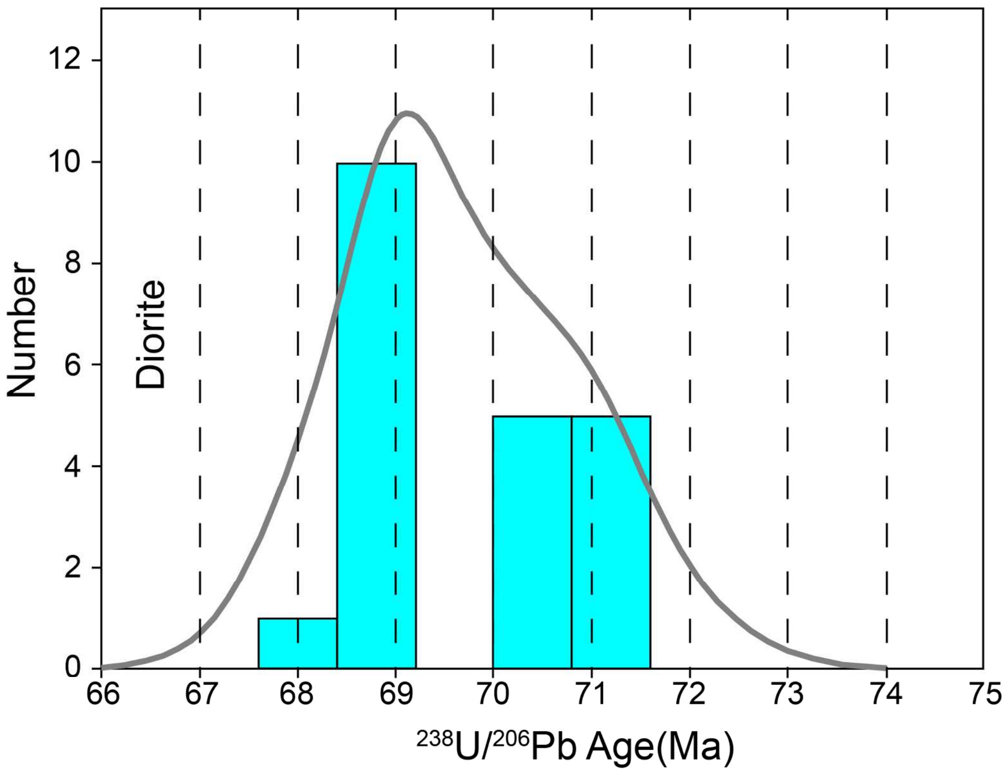

Fig. 18. Zircon U-Pb 238U/206Pb age histogram and relative probability curve for the diorite sample (NT090).

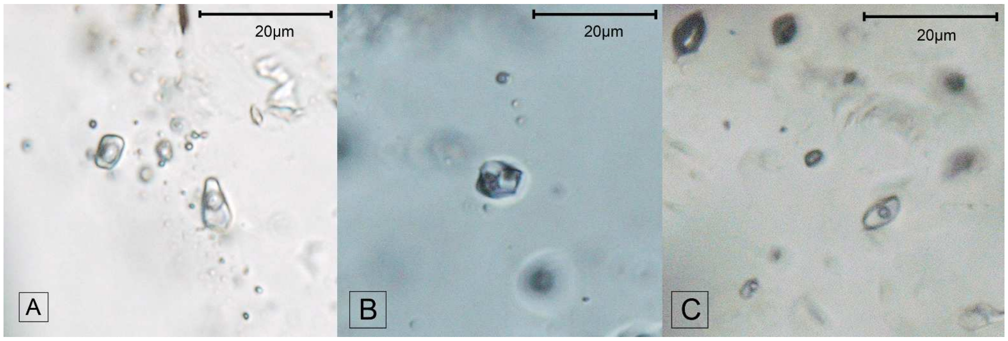

Fig. 19. Transmitted light photomicrographs showing primary fluid inclusions from stage 1 mineralization: (A) type 1 fluid inclusion assemblage from a quartz-pyrite vein (NT049); (B) type 3 primary multi-phase inclusion (liquid-vapor-halite/opaque mineral) from a quartz-molybdenite-pyrite vein (NT060); (C) type 1 liquid-rich inclusion with type 2 vapor-rich inclusions in a primary fluid inclusion assemblage from a quartz-pyrite vein (NT049).

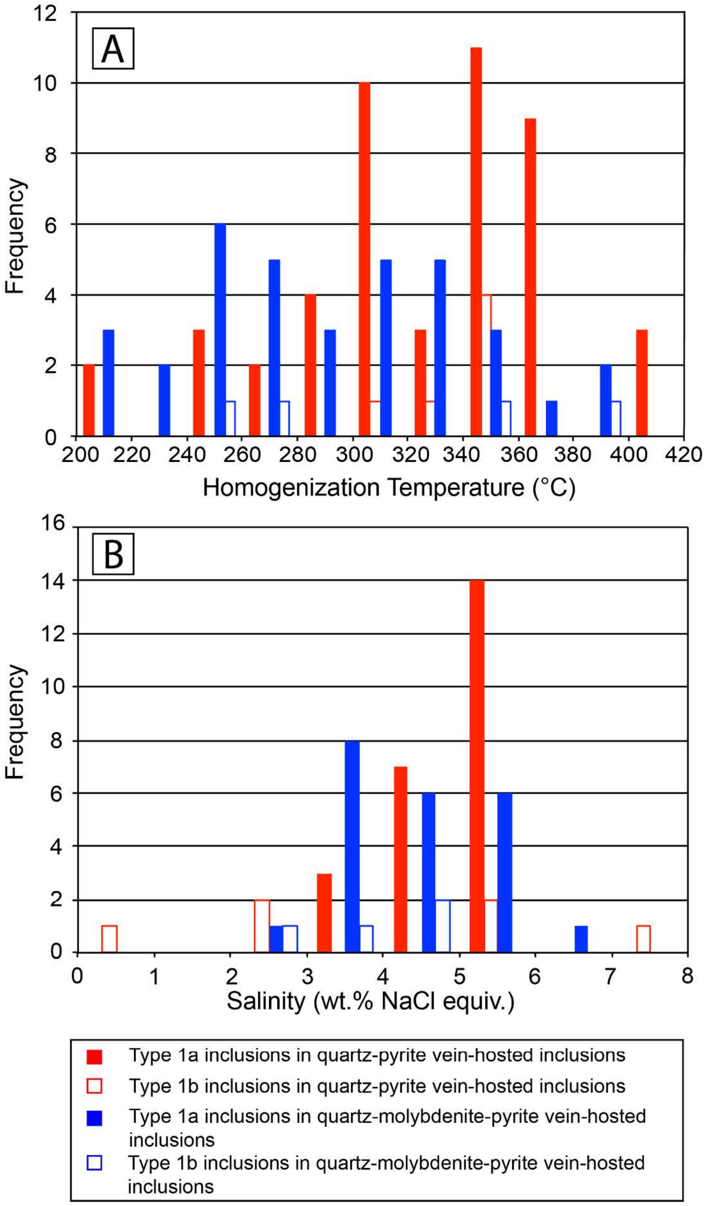

Fig. 20. Histograms showing homogenization temperature and salinity distribution for type 1 fluid inclusions from quartz-pyrite (NT049) and quartz-molybdenite-pyrite (NT060) veins.

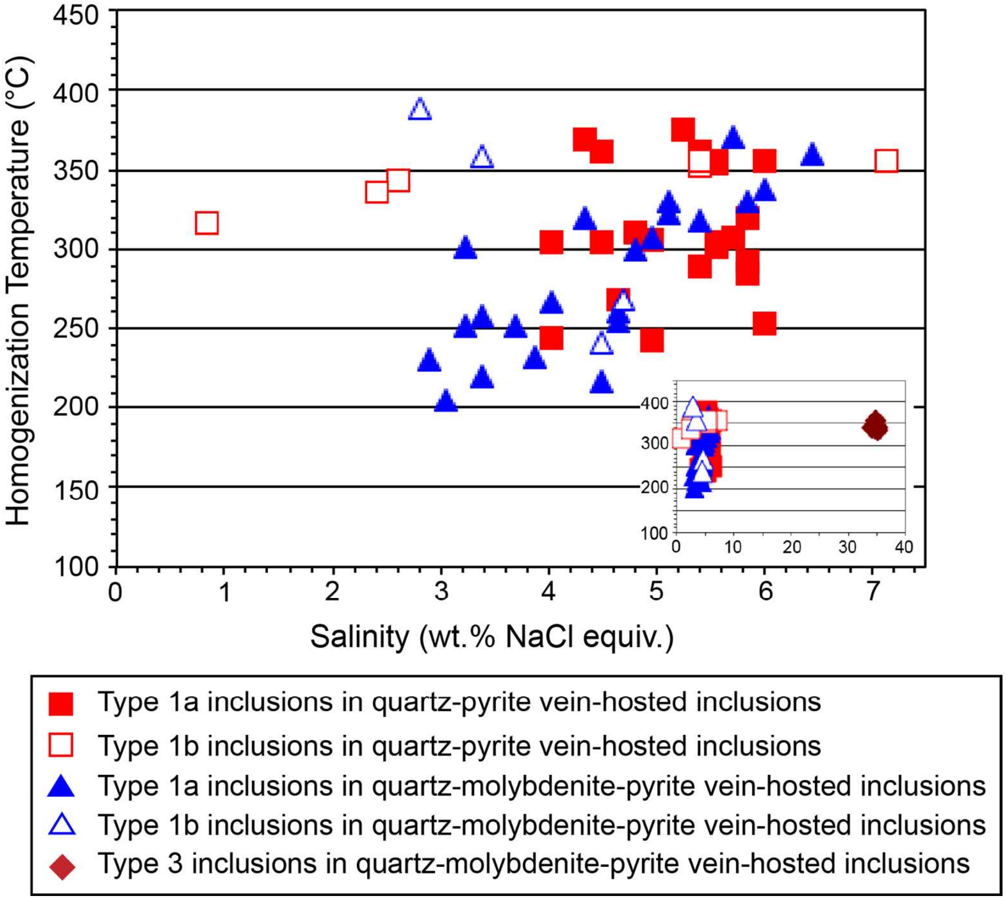

Fig. 21. Salinity versus homogenization temperature plot for inclusions from quartz-pyrite (NT049) and quartz-molybdenite-pyrite (NT060) veins.

Table 1. Major and trace element analyses of igneous rock samples from the Newton gold

Sample ID	NT038	NT047	NT056	NT059	NT066	NT090
Rock-type	Feldspar-quartz-hornblende porphyry	Feldspar-quartz-hornblende porphyry	Diorite	Feldspar-quartz-hornblende porphyry	Diorite	Diorite
Alteration	Quartz-sericite	Quartz-sericite	Weak potassic	Quartz-sericite	Weak propylitic	Weak potassic
wt.%						
SiO_2	69.76	66.64	64.34	65.04	61.04	59.37
Al_2O_3	14.80	14.44	15.14	13.14	15.74	15.55
Fe_2O_3	3.80	2.18	6.20	8.91	6.61	6.74
CaO	0.32	3.62	3.89	0.25	3.73	3.57
MgO	0.55	0.70	2.10	0.30	2.10	2.75
Na_2O	0.13	1.44	3.33	0.17	3.04	3.22
K_2O	3.80	3.47	1.78	3.91	2.53	2.05
TiO_2	0.25	0.23	0.64	0.21	0.65	0.72
P_2O_5	0.09	0.09	0.11	0.08	0.27	0.28
MnO	0.01	0.03	0.07	0.02	0.06	0.04
LOI	4.48	5.36	1.66	6.28	4.22	4.39
Total	97.99	98.20	99.26	98.31	99.99	98.68
ppm						
Cs	2.0	2.5	3.1	0.6	1.8	2.7
Tl	1.02	0.85	0.76	1.23	1.31	0.82
Rb	80	52	47	88	69	53
Ba	1069	869	1232	773	1028	924
Th	6.52	6.25	3.09	5.80	4.32	4.20
U	1.91	3.58	1.74	1.76	2.18	2.25
Nb	6.4	6.6	3.9	6.4	5.6	5.7
Ta	0.61	0.62	0.26	0.59	0.37	0.42
La	18.1	15.3	10.8	18.5	20.5	19.1
Ce	33.2	29.1	22.4	32.1	37.2	37
Pr	3.79	3.52	3.05	3.72	4.97	4.74
Sr	28	108	310	26	633	611
P	393	393	480	349	1178	1222
Nd	12.5	13.4	13	12.9	19.4	18.3
Zr	101	116	97	102	110	115
Hf	2.6	2.9	2.5	2.7	2.6	2.8
Sm	2.11	2.3	3.41	1.99	3.72	3.55
Eu	0.55	0.61	0.87	0.70	0.95	1.10

Ti	1498	1402	3824	1283	3884	4327
Gd	1.33	1.67	3.52	1.37	2.83	2.51
Tb	0.19	0.24	0.58	0.17	0.44	0.33
Dy	1.06	1.31	3.73	0.94	2.43	1.75
Y	5	8	22	5	13	9
Ho	0.20	0.24	0.78	0.17	0.45	0.33
Er	0.59	0.70	2.25	0.51	1.23	0.91
Tm	0.10	0.11	0.34	0.08	0.18	0.13
Yb	0.72	0.78	2.29	0.59	1.24	0.81
Lu	0.12	0.13	0.35	0.11	0.20	0.13

leposit			
NT097	NT129	NT134	NT137
Feldspar-quartz-hornblende porphyry	Feldspar-quartz-hornblende porphyry	Diorite	Diorite
Quartz-sericite	Quartz-sericite	Weak propylitic	Weak propylitic
66.39	62.57	56.56	65.17
13.52	14.45	15.84	15.46
4.58	4.34	7.63	6.35
2.04	2.82	4.01	4.50
0.94	1.41	3.26	1.63
1.28	3.37	2.34	3.26
5.18	2.91	3.15	1.62
0.25	0.47	0.83	0.65
0.07	0.17	0.32	0.11
0.09	0.03	0.04	0.07
5.21	5.74	5.41	1.17
99.54	98.27	99.39	99.99
2.2	2.3	5.8	1.6
1.26	0.78	1.30	0.62
99	64	72	42
1739	1075	1620	846
5.88	6.00	3.46	3.10
2.82	3.36	2.44	1.72
5.5	5	5.7	3.8
0.55	0.53	0.40	0.28
21	16.7	19.4	11.2
38	30.2	39	23.8
4.43	3.62	5.04	3.22
169	467	1021	327
306	742	1397	480
15.5	13.8	20.3	13.6
92	107	103	103
2.5	2.6	2.4	2.7
2.51	2.49	3.76	3.42
0.66	0.72	1.24	0.87

1468	2799	4951	3920
1.55	1.75	2.79	3.58
0.22	0.25	0.36	0.62
1.21	1.35	1.93	3.86
6	8	9	24
0.22	0.25	0.36	0.79
0.66	0.74	0.98	2.37
0.11	0.11	0.14	0.37
0.73	0.74	0.88	2.44
0.11	0.12	0.13	0.37

Table 2. Ziron U-Pb data for feldspar-quartz-hornblende porphyry and diorite from Newto

Sample name	^{207}Pb/^{206}Pb	2 s	^{206}Pb/^{238}U	2 s	^{206}Pb/^{238}U age (Ma)
Feldspar-quartz-hornblende porphyry					
NT_129_1	0.05077	0.00080	0.01121	0.00023	72
NT_129_2	0.05356	0.00154	0.01138	0.00029	73
NT_129_3	0.05106	0.00087	0.01105	0.00024	71
NT_129_4	0.05166	0.00115	0.01123	0.00023	72
NT_129_5	0.05474	0.00101	0.01113	0.00032	71
NT_129_6	0.06242	0.00234	0.01141	0.00026	73
NT_129_7	0.04871	0.00060	0.01145	0.00028	73
NT_129_8	0.06386	0.00247	0.01144	0.00026	73
NT_129_9	0.05521	0.00284	0.01118	0.00024	72
NT_129_10	0.05589	0.00183	0.01145	0.00025	73
NT_129_11	0.05312	0.00115	0.01140	0.00033	73
NT_129_12	0.05129	0.00096	0.01146	0.00030	73
NT_129_13	0.05335	0.00094	0.01131	0.00027	72
NT_129_14	0.05565	0.00136	0.01150	0.00039	74
NT_129_15	0.05043	0.00084	0.01138	0.00031	73
NT_129_16	0.05586	0.00182	0.01168	0.00034	75
NT_129_17	0.05028	0.00095	0.01178	0.00037	75
NT_129_18	0.05577	0.00155	0.01172	0.00034	75
NT_129_19	0.05741	0.00228	0.01142	0.00035	73
NT_129_20	0.05203	0.00095	0.01119	0.00031	72
NT_129_21	0.05503	0.00108	0.01125	0.00032	72
NT_129_22	0.05556	0.00141	0.01110	0.00033	71
NT_129_23	0.05731	0.00168	0.01124	0.00029	72
NT_129_24	0.04910	0.00066	0.01121	0.00032	72
NT_129_25	0.05003	0.00079	0.01130	0.00030	72
Diorite					
NT090_1	0.04870	0.00087	0.01091	0.00026	70
NT090_2	0.04660	0.00099	0.01092	0.00031	70
NT090_3	0.04769	0.00078	0.01101	0.00025	71
NT090_4	0.04807	0.00131	0.01084	0.00023	69
NT090_5	0.04816	0.00090	0.01097	0.00018	70
NT090_6	0.04803	0.00088	0.01075	0.00021	69
NT090_7	0.04825	0.00101	0.01080	0.00031	69
NT090_8	0.04791	0.00070	0.01078	0.00020	69

NT090_9	0.05956	0.00259	0.01104	0.00032	71
NT090_10	0.05262	0.00113	0.01097	0.00025	70
NT090_11	0.05189	0.00085	0.01079	0.00030	69
NT090_12	0.05408	0.00102	0.01105	0.00027	71
NT090_13	0.05585	0.00175	0.01074	0.00031	69
NT090_14	0.05024	0.00082	0.01098	0.00024	70
NT090_15	0.07272	0.00575	0.01104	0.00025	71
NT090_16	0.05321	0.00104	0.01066	0.00021	68
NT090_17	0.05167	0.00087	0.01078	0.00024	69
NT090_18	0.05332	0.00092	0.01070	0.00024	69
NT090_19	0.05753	0.00191	0.01082	0.00027	69
NT090_20	0.05260	0.00093	0.01072	0.00018	69
NT090_21	0.05036	0.00074	0.01108	0.00021	71

n
2 s error (Ma)
1
2
2
1
2
2
2
2
2
2
2
2
2
3
2
2
2
2
2
2
2
2
2
2
2
2
2
2
1
1
1
2
1

2
2
2
2
2
2
2
1
2
2
2
1
1

Table 3 Comparison of Newton to other intermediate-sulfidation epithermal dep

	Characteristics of intermediate sulfidation deposits (Sillitoe and Hedenquist 2003)
Genetically related volcanic rocks	Principally andesite to rhyodacite and locally rhyolite
Mineralization style	Veins and breccias, minor disseminations
Key alteration minerals	Sericite; adularia generally uncommon
Silica gangue	Vein-filling crustiform and comb quartz
Carbonate gangue	Common in veins, typically including manganiferous varieties
Other gangue	Barite and manganiferous silicates present locally
Sulfide abundance	5–>20 vol.%
Key sulfide minerals	Sphalerite, galena, tetrahedrite-tennantite, chalcopyrite
Main metals	Ag-Au, Zn, Pb, Cu
Minor metals	Mo, As, Sb

osits described by Sillitoe and Hedenquist (2003)

Characteristics of the Newton deposit
Rhyodacite to rhyolite
Disseminated
Sericite
Quartz veins are not well developed
Carbonate is only associate with stage 3 polymetallic-sulfide veins
Rare
~5–10 vol.%
Pyrite, marcasite, sphalerite, galena, and minor chalcopyrite
Ag-Au, Zn, Pb
Mo, As